FILE COPY

(2)

AD-A201 406

REPORT DOCUMENTATION PAGE

DTIC ELECTE OCT 19 1988 S D

1a. RESTRICTIVE MARKINGS: Unclassified	1b. RESTRICTIVE MARKINGS
2a. SECURITY CLASSIFICATION AUTHORITY	3. DISTRIBUTION / AVAILABILITY OF REPORT: Approved for public release; distribution unlimited.
2b. DECLASSIFICATION / DOWNGRADING SCHEDULE	
4. PERFORMING ORGANIZATION REPORT NUMBER(S)	5. MONITORING ORGANIZATION REPORT NUMBER(S): ARO 22401.1-PH
6a. NAME OF PERFORMING ORGANIZATION: Mass. Institute of Technology	6b. OFFICE SYMBOL (If applicable)
7a. NAME OF MONITORING ORGANIZATION: U. S. Army Research Office	
6c. ADDRESS (City, State, and ZIP Code): 77 Massachusetts Avenue, Cambridge, MA 02139	7b. ADDRESS (City, State, and ZIP Code): P. O. Box 12211, Research Triangle Park, NC 27709-2211
8a. NAME OF FUNDING / SPONSORING ORGANIZATION: U. S. Army Research Office	8b. OFFICE SYMBOL (If applicable)
9. PROCUREMENT INSTRUMENT IDENTIFICATION NUMBER: DAAG29-85-K-0057	
8c. ADDRESS (City, State, and ZIP Code): P. O. Box 12211, Research Triangle Park, NC 27709-2211	10. SOURCE OF FUNDING NUMBERS: PROGRAM ELEMENT NO. / PROJECT NO. / TASK NO. / WORK UNIT ACCESSION NO.

11. TITLE (Include Security Classification)

Photorefractive Effect in Barium Titanate Crystals - UNCLASSIFIED

12. PERSONAL AUTHOR(S)

A. Linz and H. P. Jenssen

13a. TYPE OF REPORT	13b. TIME COVERED	14. DATE OF REPORT (Year, Month, Day)	15. PAGE COUNT
Final	FROM Feb. 18 '85 TO May 31 '88	August 15, 1988	62 pp

16. SUPPLEMENTARY NOTATION

The view, opinions and/or findings contained in this report are those of the author(s) and should not be construed as an official Department of the Army position, policy, or decision, unless so designated by other documentation.

17. COSATI CODES		
FIELD	GROUP	SUB-GROUP

18. SUBJECT TERMS (Continue on reverse if necessary and identify by block number)

Chemical Purification ~~of $BaCO_3$~~ and TiO_2; Crystal growth ~~of $BaTiO_3$~~; Photorefractive effect, ~~in $BaTiO_3$~~; and Iron doped $BaTiO_3$

19. ABSTRACT (Continue on reverse if necessary and identify by block number)

Variable-valent iron impurities have been suggested as the source of photorefractive charge carriers in $BaTiO_3$. Very high-purity $BaTiO_3$ crystals were grown with transition-metal impurity levels below the $10^{16} cm^{-3}$ baseline estimate for photorefractivity. Iron-doped crystals also were grown with concentrations of 5, 50, 250, 500, 750, and 1000 ppm Fe. Changes in iron valence monitored by optical absorption in the P_{O_2} range 1 to 10^{-4} atm were found to be consistent with a defect-chemical model indicating Fe^{3+} and Fe^{4+} to be the characterization of high-purity $BaTiO_3$ suggests that variable-valent iron ions are not the dominant photorefractive species in these crystals, while the role of iron centers in doped crystals is complicated by large absorption losses.

A study of some growth problems effecting purity and perfection of TSSG $BaTiO_3$ crystals was performed. Some preliminary growth experiments in an rf heated Czochralski furnace indicated that it might be possible to utilize the cleaner growth environment of this type of equipment for $BaTiO_3$. Studies were also conducted to investigate the problem of "capping" after seeding in the TSSG process. It was concluded that convective instabilities in the melt were probably the limiting factor.

20. DISTRIBUTION / AVAILABILITY OF ABSTRACT	21. ABSTRACT SECURITY CLASSIFICATION	
☐ UNCLASSIFIED/UNLIMITED ☐ SAME AS RPT. ☐ DTIC USERS	Unclassified	
22a. NAME OF RESPONSIBLE INDIVIDUAL	22b. TELEPHONE (Include Area Code)	22c. OFFICE SYMBOL

DD FORM 1473, 84 MAR — 83 APR edition may be used until exhausted. All other editions are obsolete.

SECURITY CLASSIFICATION OF THIS PAGE: UNCLASSIFIED

88 10 18 01

PHOTOREFRACTIVE EFFECT IN BARIUM TITANATE CRYSTALS

Final Report

by

A. Linz and H. P. Jenssen

August 15, 1988

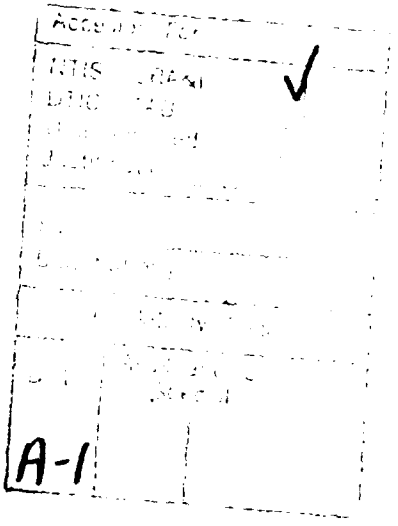

Submitted to:
U. S. Army Research Office

Contract Number
DAAG29-85-K-0057

From:
MASSACHUSETTS INSTITUTE OF TECHNOLOGY

PHOTOREFRACTIVE EFFECT IN BARIUM TITANATE CRYSTALS

I. Program Summary

The main goal of this program was to identify, control and optimize the centers responsible for the photorefractive effect in $BaTiO_3$. To this end, we grew both very high purity and iron doped crystals of $BaTiO_3$ using the top seeded solution growth (TSSG) method. These materials were studied extensively using both optical absorption measurements and photorefractive characterization techniques both before and after anneals in various partial pressures of oxygen. The details of this investigation and the results obtained are presented in section II of this report. While we did not succeed completely in achieving our goal of identifying photorefractive centers in $BaTiO_3$, it does appear that the popular Fe^{2+}/Fe^{3+} model does not apply and that the defects are more likely to be barium and/or oxygen ion vacancies.

Two aspects of the crystal growth procedure which presented some problems during the course of this research were also briefly investigated as described in section III. The interior of our SiC heated furnaces is of necessity a less clean environment than can be arranged in an RF heated Czochralski furnace, so some preliminary growth runs were made in the latter unit. Temperature and gradient control were not optimized, but there were indications that with further study $BaTiO_3$ growth in this furnace might be feasible.

The problem that most affects TSSG, occasionaly causing cracking and strain, is the tendency for a cap to form underneath the seed. This is a well known phenomenon in solution growth and in the time remaining in this program efforts were made to find ways of minimizing it. While some success was achieved this basic controlling factor appears to be convectional instabilities in the melt leading to constitutional supercooling at the very small seed melt interface.

II. The Role of Iron Centers in the Photorefractive Effect in $BaTiO_3$

P.G. Schunemann,* D.A. Temple, R.S. Hathcock, H.L. Tuller,
H.P. Jenssen, D.R. Gabbe and C. Warde
Crystal Physics and Optical Electronics Laboratory
Massachusetts Institute of Technology, Cambridge, MA 02139

ABSTRACT

Variable-valent iron impurities have been suggested as the source of photorefractive charge carriers in $BaTiO_3$. High-purity $BaTiO_3$ crystals were grown with transition-metal impurity levels below the $10^{16}cm^{-3}$ baseline estimated for photorefractivity. Iron-doped crystals were grown with concentrations of 5, 50, 250, 500, 750, and 1000ppm Fe. Changes in iron valence monitored by optical absorption in the P_{O2} range 1 to 10^{-4} atm were found to be consistent with a defect-chemical model indicating Fe^{3+} and Fe^{4+} to be the stable valence states in this range. Photorefractive characterization of high-purity $BaTiO_3$ suggests that variable-valent iron ions are not the dominant photorefractive species in these crystals, while the role of iron centers in doped crystals is complicated by large absorption losses.

*currently at Sanders Associates, 130 Daniel Webster Highway, Merrimack, NH 03054

to be published in J. Opt. Soc. Am. B. (August 1988)

INTRODUCTION

$BaTiO_3$ is of particular interest among photorefractive materials because it has demonstrated the highest four-wave-mixing reflectivities (greater than a factor of 20) by virtue of its large electro-optic coefficients.[1,2] Despite barium titanate's promise for applications involving phase conjugation and optical information processing, the centers responsible for the photorefractive effect in this material have not been conclusively identified, and this lack of understanding hinders the control and optimization of its non-linear optical and phototefractive properties.

The basic physics of the photorefractive effect is by now well understood[3]: (1) upon non-uniform illumination of the material, carriers (electrons or holes) are optically excited from energy levels (donors or acceptors) in the band gap; (2) the excited carriers migrate by diffusion and drift and are re-trapped and re-excited until they reach the less bright regions of the material; and (3) this redistribution of charge creates internal electric fields that modulate the refractive index of the material via the electro-optic effect. The exact identity of the photorefractive sources and traps, however, remains unclear for $BaTiO_3$.

Previous efforts to isolate the photorefractive centers in $BaTiO_3$ have focussed mainly on nominally undoped crystals from a single commercial source.[4] Klein and Schwartz[5]

determined the impurity concentrations in a series of such crystals by chemical analysis and noted a general increase in the photorefractive trap density, Fe^{3+} EPR signal, and absorption coefficient with increasing iron content over a narrow concentration range (~50-150ppm). Based on their observations and on similar results reported for $LiNbO_3$,[6-9] they concluded that Fe^{3+} and Fe^{2+} were the sources and traps respectively of photorefractive carriers when the carriers are holes (and vice-versa for electrons). Reduction of these same crystals (P_{O2}= $10^{-8.1}$ to 10^{-12} atm) yielded increases in photorefractive speed and a change in carrier sign from positive to negative that were explained by a model based on variations in the Fe^{2+}/Fe^{3+} ratio.[10] Ducharme and Feinberg[11] reported the effects of oxidation and reduction at 650°C on a nominally undoped crystal, and also noted a change in photorefractive carrier sign, which in their crystal corresponded to a minimum in trap density around 0.5 atm. These results led them to conclude that oxygen vacancies (or impurity-oxygen vacancy complexes) were the photorefractive donors of negative charge.

The only reported study of the photorefractive properties of intentionally doped $BaTiO_3$ is the recent work of Godefroy et al.[12] They measured the maximum diffraction efficiency, writing speed, and electro-optic coefficients in a series of crystals doped with a wide range of Fe concentrations (undoped to 2500ppm). They reported that all measured parameters were highest in the 750ppm Fe-doped

crystal, with the diffraction efficiency increasing by a factor of 1000 over that of the undoped crystal. A major shortcoming of this work, however, is that the measured crystals were neither electrically nor mechanically poled, and the measurements they performed are particularly sensitive to the presence of 90 and 180 degree domains. In fact, their reported investigations of the crystal domain structure (performed using a unique optical topography approach) indicated a low degree of poling and notable variation among crystals.

The goal of this research was to gain more insight into the role of iron centers, if any, in the photorefractive process in barium titanate by controlling the concentration and valence states of the iron in a series of crystals and correlating the results with measured optical and photorefractive properties. Our approach is based on the popular theory[5] that variable-valent transition-metal ions, in particular divalent and trivalent iron impurities, are the species responsible for photorefractive charge carriers in barium titanate.

Our strategy for evaluating the effects of such centers on the photorefractive behavior of barium titanate was four-fold. Since it has been estimated that the density of charge carriers involved in the photorefractive effect is on the order of $10^{16}/cm^3$,[13] the first goal of this research was to prepare high purity single crystals with transition-metal and aliovalent impurity levels below this level. The

second goal of this work was to grow a series of Fe-doped $BaTiO_3$ single crystals with low background impurity levels by systematically doping the melt from which the above-mentioned high purity crystals were grown. Thirdly, we employed a defect chemical approach to control the iron valence via thermal oxidation and reduction treatments. Finally, these variations in iron concentration and valence were correlated with general trends in the photorefractive behavior of the crystals as characterized by saturation diffraction efficiency, light-induced grating erasure rate, and two-beam coupling measurements. Preliminary results of this study have recently been presented.[14-16]

HIGH PURITY $BaTiO_3$ SYNTHESIS

Purification of Starting materials

A major effort in this research was devoted to the synthesis of high-purity starting materials, since titanium dioxide and barium carbonate feed materials are not commercially available with impurity levels below the nominal concentration of $10^{16}/cm^3$ that is apparently required for photorefractivity.

The titanium dioxide feed material was prepared by the hydrolysis of titanium isopropoxide, $Ti(^iOC_3H_7)_4$, according to the reaction

$$Ti(^iOC_3H_7)_4 + 3H_2O \xrightarrow{C_3H_7OH} TiO_2 \cdot H_2O + 4C_3H_7OH \quad (1)$$

The titanium alkoxide precursor (Stauffer Chemical Co.) was first purified by a reduced pressure fractional distillation. This purification technique was based on the observation that titanium isopropoxide has a much lower boiling point than the isopropoxides of other transition-metal impurities.[17] A 600mm x 12.5mm vacuum-jacketed distilling column packed with 1/8" glass helices provided ~15-20 "theoretical plates."[18] Purification was qualitatively evidenced by the transformation of the alkoxide from deep-yellow to water-clear in color, leaving a dark-brown liquid and metal particulates in the still pot. The collected distillate was removed under a dry-nitrogen atmosphere and reacted with a dilute solution of deionized water and semiconductor-grade isopropyl alcohol (Mallinkrodt) to form hydrated TiO_2 powder which was then vacuum-dried in the same vessel. A flow chart for the process is shown in Figure 1 (a).

Barium Carbonate was formed by reaction of a purified aqueous solution of $BaCl_2$ and urea with CO_2 in a pressurized vessel. Reagent grade $BaCl_2$ and urea, $(NH_2)_2CO$, were dissolved in water, filtered, and purified by solvent extraction. In the solvent extraction process, the aqueous solution was intimately mixed with a dense immiscible liquid phase (chloroform) which contained an extracting or "chelating" agent (diethylammonium diethyldithiocarbonate, DDDC) which readily forms complexes with a large number of metal ions. These metal complexes segregated to the dense

chloroform phase, where their presence was indicated by a bright yellow or green color, and were subsequently removed using a separatory funnel. The extraction process was repeated for several solution pH's until the extracting phase was colorless. After extraction, the purified solution was refiltered and reacted under CO_2 pressure (150 psi, ~80°C) to form crystalline $BaCO_3$ which was centrifuged, washed, and dried. A flow chart for the entire process, carried out in a class 100 clean room, is shown in Figure 1(b).

Single Crystal Growth

High-purity $BaTiO_3$ single crystals were grown by the top-seeded solution growth technique (TSSG).[19,20] Extreme care was exercised to minimize furnace contamination of the purified feed materials. The growth furnace was rebricked with new lining materials, new SiC heating elements were used, and the platinum crucible was kept covered while the closing bricks were lowered in place. Crystal growth was first initiated on a platinum wire to avoid contamination from an impure single-crystal seed. Later, high-purity single-crystal seeds cut in the <100> direction were used with dimensions of approximately 10 x 2.5 x 2.5mm.

Single crystals were grown from a titanium rich melt containing 66 mole% TiO_2 corresponding to a liquidus temperature of approximately 1380°C. (Experience has indicated that growth from melts at temperatures > 1400°C

yields poor results.) The melt was heated slowly at first to drive out moisture, then raised from 200 to 1450°C in 20 hours and soaked for 24 to 40 hours to insure complete dissolution of the ceramic powders. Seeding temperatures, indicated by equilibrium between the melt and the air-cooled seed, varied between 1382°C and 1392°C for successful growth runs due to variations in the moisture content of the hydrated TiO_2. After seeding, the melt was cooled at 0.2°C/hour for 25 to 35 hours until pulling began at 0.15 to 0.2mm/hour. During pulling the melt was cooled at 0.5°C/hour to temperatures slightly above the eutectic (1320°C), after which the crystal was removed from the melt and slowly cooled to room temperature. Most growth runs yielded single crystal boules of good optical quality as shown in Figure 2.

Optical Sample Preparation

Crystals were cut along (100) planes as determined by the back-reflection Laue method, and faces were ground to near-parallel with 20μm SiC. Cut and ground cubes were then polished by hand with 3 μm diamond paste on a lightly-oiled paper lap. The presence of 90° domains in the polished samples was clearly indicated by sharp planar boundaries within the polished samples which ran diagonally across the predominantly a-faces, as shown in Figure 3. These domain walls, in fact, served to identify the a-faces, while the c-direction was indicated by a characteristic color pattern when viewed between crossed polarizers.

Single domain samples were achieved by a combination of mechanical and electrical poling. Uniaxial stresses of 1500 to 3000 psi applied along an a-axis were generally sufficient to remove all visible 90° domain walls. During application of the stress, performed using a pressurized piston, the 90° domain walls visible in the unstressed a-direction would migrate towards the corners of the crystal. This migration would create surface steps on faces along which the ends of the domain wall boundaries moved. The moving domain walls would eventually get hung-up on these surface steps so that the crystal needed to be repolished before poling could continue. After sufficient iterations all directly visible 90° domain walls could be removed, although a cloudiness visible in crossed polarizers often revealed the presence of residual 90° domains. These were removed upon application of an applied field of 1000V/cm in an oil bath near or above the Curie temperature (133°C). Nickel electrodes were polished to optical flatness to ensure good electrical contact, and voltage was applied slowly (10V/min) to reduce the tendency toward surface cracking at the positive electrode which sometimes occurs during rapid domain re-orientation.

Critical factors in achieving poled $BaTiO_3$ samples proved to be (1) having a good polish so that moving domain walls would not hang up on surface flaws, (2) using multiple iterations during mechanical poling to avoid stressing and cracking, and (3) having stress-free single-

crystals. Residual stresses from cooling through the phase transition during crystal growth, or stresses induced during mechanical polishing and poling could sometimes prevent complete mechanical poling and would often cause severe cracking during electrical poling.

Evaluation of Sample Purity

A combination of spark-source mass spectrometry (Northern Analytical Laboratory, Amherst, New Hampshire), ultraviolet spectrophotometry, and optical absorption spectroscopy were used to confirm the impurity concentration levels in the starting materials, the purified feed, and the resulting high-purity $BaTiO_3$ single crystals. The results of spark-source mass spectrometry are listed in Table 1, and the UV spectrophotometric data and visible absorption spectra are given in Figures 4 and 5 respectively. The results of these analyses can be summarized as follows:

(1) The spark-source data indicated that the titanium dioxide fractional distillation procedure reduced the iron content by a factor of four and removed all other transition metals to below detection limits;

(2) UV spectrophotometric data of purified $BaCO_3$ and the reagent $BaCl_2$ precursor dissolved in HCl (Figure 4) indicated that the absorbance due to transition-metal chlorocomplexes in the $BaCO_3$ is significantly lower than in the $BaCl_2$. The peak at 230nm in the $BaCl_2$ spectra corresponds well to the iron peak reported in the literature.[21] In contrast, then, to the mass spectrometric

data, which gave Fe concentrations of 0.3 and 1ppm in $BaCl_2$ and $BaCO_3$ respectively, these results show that the $BaCO_3$ purification process significantly reduced the Fe levels of the $BaCl_2$ precursor;

(3) Optical absorption spectra of crystals grown from (a) reagent $BaCO_3$ and Baker ULTREX^{TM} TiO_2, (b) reagent grade $BaCO_3$ and purified TiO_2, and (c) purified $BaCO_3$ and purified TiO_2 synthesized in this laboratory (Figure 5) reveal that the band edge of the high-purity crystal is shifted to a slightly shorter wavelength and drops off more steeply, both indications of decreased impurity levels;

(4) As indicated by mass spectrometry, transition metal impurity levels in the high-purity $BaTiO_3$ single crystal are near or below the nominal concentration of $10^{16}/cm^3$ (1ppma = $1.56x10^{16}/cm^3$) predicted for observing the photorefractive effect. Iron and nickel were measured at concentrations of 0.3 and 0.04ppm (atomic) respectively, while all other transition metals were below detection limits (0.01ppm). The only aliovalent impurities reported at levels greater than this were B (5ppm), Al (0.5ppm), and Cl (10ppm), a remnant of the barium chloride precursor. These results reveal these high purity $BaTiO_3$ crystals to be the purest yet achieved in this laboratory or ever used for photorefractive studies.

SYSTEMATIC IRON DOPING

In order to systematically investigate the effects of iron concentration on the photorefractive properties of $BaTiO_3$, crystals were grown from melt compositions containing 5, 50, 250, 500, 750, and 1000ppm Fe. Doping was accomplished by substituting iron oxide for TiO_2 in the above-mentioned high-purity melt according to 34% $BaCO_3$ + 66% $[(1-x)TiO_2 + (x/2)Fe_2O_3]$, where x is the doping level in ppm (atomic). The iron concentration, therefore, refers to the ratio Fe/Ti in the melt. The actual iron concentrations in the resulting crystals were confirmed by chemical analysis. Atomic Absorption analysis (Northern Analytical Laboratories, Amherst, NH) was conducted on the doped $BaTiO_3$ samples which were dissolved by fusing with lithium tetraborate. The results are listed in Table 2 and indicate a segregation coefficient near unity. This value for the segregation coefficient is somewhat higher than that reported by Godefroy et al[22] for TSSG $BaTiO_3$. Their iron concentrations, however, were substantially higher than those used in this study, and the few data points at lower concentrations do suggest values approaching unity.

Single domain optical samples of the Fe-doped crystals were prepared as described previously for the case of high purity crystals except that two notable differences in behavior were observed during the electrical poling procedure. First, crystals containing 500, 750, and 1000ppm Fe were found to develop an unusual bright yellow color band

during application of the applied field (1000V/cm) at temperatures near the Curie temperature, T_c. This color band was defined by a sharp boundary parallel to the positive electrode, and with time this boundary propogated towards the negative electrode. A similar coloration phenomenon was apparently observed by Godefroy et al[12] and prevented them from electrically poling their samples. Fortunately in these experiments the color front advanced only 1 or 2mm into the crystal in the times required for electrical poling (1.5 to 2.5 hours), thereby leaving a large enough region for optical evaluation.

Electrocoloration phenomena have been previously reported in both $BaTiO_3$[23,24] and $SrTiO_3$.[25] Blanc and Staebler[25] noted that the application of dc electric fields to transition-metal-doped strontium titanate in the temperature range of ~100-325°C resulted in the appearance of colored regions characteristic of oxidized material at the positive electrode and reduced material at the negative electrode. Their results were consistent with a simple model based on the drift of doubly-ionized oxygen vacancies under the influence of the applied field which caused oxidation and reduction of stationary transition metal ions near the positive and negative electrodes respectively. This effect was observed for all transition metals studied: Fe, Ni, Co, and Mo. Assuming the same phenomenon occurs in our heavily doped $BaTiO_3$:Fe samples, we applied their

analysis to our results to obtain an approximate value for the mobility of oxygen vacancies μ_V in $BaTiO_3$ given by

$$dx/dt = \mu_V V/x \qquad (2)$$

where dx/dt is the rate of the color boundary movement, x is the width of the untransformed region, and V is the applied voltage. This yielded a μ_V value of ~$3\times10^{-8}cm^2$/volt-sec at ~128°C, which compares favorably with the $1.5\times10^{-8}cm^2$/volt-sec obtained by Blanc and Staebler[25] for $SrTiO_3$ at 200°C.

The second effect of added Fe which was noted during electrical poling was a slight decrease in the Curie temperature evidenced by visual observation of the tetragonal-to-cubic phase transition. More accurate Curie temperature measurements were performed using capacitance techniques on thin (100) slabs cut from high-purity, 50, 500, and 1000ppm Fe-doped samples. These samples were equilibrated at 800°C in oxygen partial pressures of 1, 10^{-2}, and 10^{-4} atm, and in each case subsequently quenched to ~175°C and slowly cooled to ~125°C while monitoring the ac capacitance (100kHz). In each case the phase change was marked by a sudden plunge in the relative dielectric constant from ~12,000 in the cubic phase to ~2000 after the transition. The results indicated that the Curie temperature dropped about 2°C per 1000ppm Fe, in close agreement with the value of -21°C/mole% reported by Hagemann and Ihrig.[26] Annealing in the oxygen partial pressure range indicated above had no significant effect on T_c, however, in

agreement with the previous workers as well as with Weschler et al[10] but in sharp contrast to the results of Ducharme and Feinberg[11] who noted a 6°C drop in T_c for annealing in argon as compared to oxygen.

CONTROL OF IRON VALENCE

Defect Chemistry of $BaTiO_3$:Fe

The understanding and control of the various valence states of iron and their relative concentrations is clearly critical to evaluating the possible role of these centers in the photorefractive process in $BaTiO_3$. The defect chemistry of $BaTiO_3$,[27-32] and in particular transition-metal-doped $BaTiO_3$,[26,33-35] has been extensively studied by high-temperature electrical conductivity, thermogravimetry, Mossbauer spectroscopy, and electron paramagnetic resonance. The work of Hagemann et al[26,33-35] on Fe-doped $BaTiO_3$ yielded the thermodynamic defect model presented below which allows the concentrations of Fe^{2+}, Fe^{3+}, and Fe^{4+} to be determined as a function of oxygen partial pressure, temperature, and total Fe doping level.

When $BaTiO_3$ is treated at very low oxygen-partial pressures and elevated temperatures, oxygen vacancies are created and balanced by the generation of mobile electrons according to the reaction

$$O_O^X = 1/2O_2 + V_O^{\cdot\cdot} + 2e' \qquad (3)$$

with an equilibrium constant for reduction given by

$$K_n = [V_O^{\cdot\cdot}]n^2P_{O2}^{1/2} = K_n''\exp(-\Delta H_n''/kT) \qquad (4)$$

where n is the electron concentration and $\Delta H_n''$ is the standard enthalpy of reduction associated with the formation of doubly-ionized oxygen vacancies. The notation is that of Kroger and Vink,[36] where the superscript cross, dot, and slash correspond to neutral, positive, and negative effective charges respectively. The electroneutrality condition in this regime is simply

$$2[V_O^{\cdot\cdot}] = n \tag{5}$$

where the atmosphere controlled oxygen vacancy concentration is much greater than the total iron concentration.

At higher oxygen partial pressures, however, the oxygen vacancy concentration becomes fixed by the total iron concentration depending on the stable valence state(s) present. For every two Fe^{4+} ions reduced to Fe^{3+} one oxygen vacancy is formed, while for every Fe^{2+} ion formed one oxygen vacancy is generated. Consequently the condition of charge balance requires that

$$[Fe_{Ti}'] = 2[V_O^{\cdot\cdot}] \tag{6}$$

when trivalent and tetravalent iron are present or

$$[Fe_{Ti}'] + 2[Fe_{Ti}''] = 2[V_O^{\cdot\cdot}] \tag{7}$$

at lower P_{O2} where both Fe^{3+} and Fe^{2+} are present and are represented by Fe_{Ti}' and Fe_{Ti}'' respectively. The relevant ionization reactions are given by

$$Fe_{Ti}'' = Fe_{Ti}' + e' \tag{8}$$

and

$$Fe_{Ti}' = Fe_{Ti}^{X} + e' \tag{9}$$

These reactions have the corresponding mass action relations[34,35]

$$[Fe_{Ti}']n/[Fe_{Ti}''] = K_D'' = 1/2N_C\exp-(E_g-E_{Fe}^{2-})/kT \quad (10)$$

$$[Fe_{Ti}^{X}]n/[Fe_{Ti}'] = K_D' = 2N_C\exp-(E_g-E_{Fe}^{-})/kT \quad (11)$$

where N_C is the density of states in the conduction band ($1.55\times10^{22}cm^{-3}$), E_g is the band gap of $BaTiO_3$ (3.1eV), and E_{Fe}^{2-} and E_{Fe}^{-} are the energy levels of Fe^{3+} and Fe^{4+} respectively as measured from the top of the valence band.

The concentration of iron ions in a given valence state is related to the total iron concentration through the mass balance equations

$$[Fe_{Ti}]_{tot} = [Fe_{Ti}'] + [Fe_{Ti}^{X}] \quad (12)$$

or

$$[Fe_{Ti}]_{tot} = [Fe_{Ti}''] + [Fe_{Ti}'] \quad (13)$$

for oxidizing and reducing conditions respectively.

The equilibrium defect model represented by Equations (3)-(13) can be used to quantitatively predict the relative concentration levels of Fe^{2+}, Fe^{3+}, and Fe^{4+} for a given set of annealing conditions and doping levels if values for the equilibrium constants K_n'', K_D' and K_D'' are known. The equilibrium constants have been determined by thermogravimetric measurements[34,35] and high-temperature-electrical conductivity measurements,[29-32] which give $K_n'' \sim 3\times10^{75}cm^{-9}Pa^{1/2}$ and $\Delta H_n'' \sim 9.6\times10^{-19}J$. The ionization energies have been determined using thermogravimetry and Mossbauer spectroscopy by H. J. Hagemann.[35] These results yielded values for E_{Fe}^{-} and E_{Fe}^{2-} of 0.8 eV and 2.4 eV

respectively. These values inserted into Equations (4), (10), and (11) and combined with Equations (6) and (7) yield values for $[Fe^{2+}]$, $[Fe^{3+}]$, and $[Fe^{4+}]$ as a function of oxygen partial pressure and temperature. Results of such calculations for an equilibrium temperature of 800°C and the total Fe concentrations relevant to this study (0.3, 50, 500, and 1000ppm) are shown plotted in Figure 6.

A number of important trends are illustrated in Figure 6. For each Fe concentration labeled at the left of the diagram, the three plateaus going from left to right correspond to saturation of the Fe ions in the divalent, trivalent, and tetravalent states respectively with increasing P_{O2}. Note that Fe^{4+} and Fe^{3+} are the predominant species under the relatively oxidizing atmospheres encountered during crystal growth, while the Fe^{2+} concentration is extremely low ($<10^{15}cm^{-3}$) even for the highest Fe concentration and lowest P_{O2} encountered in this study (1000ppm Fe, 10^{-4} atm). The specific P_{O2}-dependent trends illustrated in Figure 6 can be derived by combining Equations (4), (7), and (10) or Equations (4), (6), and (11) and differentiating with respect to $\log P_{O2}$. Performing this analysis yields

$$d\log[Fe^{3+}]/d\log P_{O2} = -d\log[Fe^{2+}]/d\log P_{O2} = 1/4 \quad (14)$$

for low P_{O2}'s, while at higher P_{O2}'s

$$d\log[Fe^{4+}]/d\log P_{O2} = 1/4 \quad (15)$$

and

$$d\log[Fe^{3+}]/d\log P_{O2} = -1/6 \quad (16)$$

Similar manipulation of these equations with respect to the total Fe concentration $[Fe]_{tot}$ at a fixed P_{O2} yields

$$d\log[Fe^{2+}]/d\log[Fe]_{tot} = 1/2 \quad (17)$$

and $$d\log[Fe^{4+}]/d\log[Fe]_{tot} = 3/2 \quad (18)$$

(Equations 14-16 apply to the regions in Figure 6 where the concentration of a given valence state is changing, and break down as saturation is approached.) Note from Equations (17) and (18) that the concentration of a given valence state does not increase linearly with Fe content as one might intuitively expect. It is also notable that the Fe^{4+} concentration increases rather rapidly with iron content as compared with Fe^{2+}.

The above defect model governs the changes in oxygen vacancy concentration in addition to iron valence. These are plotted in Figure 7 as a function of oxygen partial pressure for the same conditions as those in Figure 6. Note that the oxygen vacancy concentration is fixed over a wide P_{O2} range by the Fe^{3+} concentration according to Equation (6). At lower P_{O2}'s, however, Equation (5) dominates Equation (7) and additional oxygen vacancies are charge-compensated by conduction electrons, resulting in high electrical conductivity. Comparison with Figure 6 reveals that this intrinsic compensation mechanism takes over before substantial Fe^{2+} can be formed. At high oxygen partial pressures, the oxygen vacancy concentration reaches a plateau determined by the level of background impurities, which in Figure 7 is determined from the chemical analysis

results in Table 1. An important consequence of the trends illustrated in Figure 7 is that oxygen vacancies can be ruled out as the donors responsible for P_{O2}-dependent changes in photorefractive properties since their concentration is fixed over a wide P_{O2} range by the presence of acceptor impurities or dopants.

Finally, although the above trends apply at room temperature, some care should be taken in applying the actual defect concentrations shown in Figure 6 to crystals at 25°C. In the case of oxygen vacancies, rapidly quenching the samples from 800°C effectively "freezes in" the high temperature ionic defect structure so that the concentrations in Figure 7 should still hold. The relative concentrations of Fe^{2+}, Fe^{3+}, and Fe^{4+}, however, depend upon the degree of ionization of defects in the system which is highly temperature dependent. Upon cooling some deionization will occur, which in the case of holes will shift the curves in Figure 6 to lower oxygen partial pressures, thus favoring the formation of higher oxidation states.

Optical Absorption Spectroscopy

The variations in iron valence governed by the above model were monitored via optical absorption measurements based on the characteristic spectra of Fe^{2+}, Fe^{3+}, and Fe^{4+} in $BaTiO_3$. Since no published absorption spectra were available for melt-grown $BaTiO_3$:Fe, results for Fe-doped

$SrTiO_3$[35] served as a guide to the interpretation of our measured spectra. In $SrTiO_3$:2300ppm Fe, Fe^{4+} charge transfer bands have been associated with an absorption peak and shoulder at 440 and 590nm respectively in oxidized samples (P_{O2} = 1 to 10^{-4} atm), giving them a reddish/brownish color.[35] Under more reducing conditions (P_{O2} = 10^{-4} to 10^{-17} atm), Fe exists almost entirely in the trivalent state, leaving the same crystals nearly colorless. Significant amounts of Fe^{2+} are formed only in heavily-reduced crystals (P_{O2} < 10^{-17}) and have been associated with a double-band with peaks at 1030 and 825nm which cause the crystals to appear greenish in color.[35]

Optical absorbance measurements of our $BaTiO_3$:Fe samples yielded similar results. These were performed using a Perkin-Elmer Lambda 9 double-beam spectrophotometer. Visible absorption spectra were measured between 380 and 860nm on as-grown and annealed samples for light polarized parallel and perpendicular to the c-axis. Automatic background correction compensated for the effects of matched polarizers and a 4mm circular beam mask. The absorption spectra of the high purity sample and of those doped with 5, 50, 250, 500, 750, and 1000ppm Fe were measured in the as-grown condition after mechanical poling, and the results are shown in Figure 8. In each case the absorption coefficient α was calculated from the measured transmission T according to

$$\alpha = [2\ln(1-R) - \ln T]/d \qquad (19)$$

where d is the sample thickness and R is the reflectance, which is related to the refractive index by

$$R = (n-1)^2/(n+1)^2 \qquad (20)$$

for the case of normal incidence.[38] Corrections for reflectance were made using Equation (20) and the refractive index data of Wemple et al[39] for $BaTiO_3$ as a function of wavelength and polarization.

In Figure 8, the effect of Fe doping on the absorption coefficient of as-grown crystals is clear. The data for $E \| c$ and $E \perp c$ are given in (a) and (b) respectively. These spectra are characterized by a broad absorption band, extending throughout the visible to the band edge, that increases with increasing Fe content. In addition, the extended band edge appears to shift to higher wavelengths with increasing Fe concentration. The $E \perp c$ polarization shows the emergence of a well-defined shoulder at 620nm for Fe levels greater than 500ppm. The slight inconsistencies in the observed trends (i.e., the intersection of the 5ppm and 250ppm data with the 50 and 500ppm curves) were due to scattering from residual 90 degree domain walls in the 5 and 250ppm samples which increased the measured absorbance. These inconsistencies were removed upon electrical poling, however not all of the samples shown survived this procedure.

A second set of samples from boules of high-purity, 50ppm Fe, 500ppm Fe and 1000ppm Fe were measured after annealing at 800°C in oxygen (1 atm) and in 100ppm O_2/Ar

(10^{-4}atm) _respectively. Oxygen partial pressures were controlled using premixed Ar-O_2 gases and monitored using a calcia-stabilized zirconia electrochemical oxygen sensor in series with the sample furnace.

Before annealing, the c-faces of the samples were painted with platinum paste and the crystals were mounted between platinum sheet electrodes in adjacent, spring-loaded sample holders. The crystals were heated slowly through the Curie temperature (4 to 6 ^{o}C/hour) and then heated to 800^{o}C in 1 hour. Samples were annealed for equilibration times based on the bulk diffusion data of Wernicke[37] (~36 hours) and subsequently quenched to just above T_c (where the oxygen diffusivity is negligible) in order to "freeze in" the high temperature defect structure. Quenching was performed by transferring the gas-sealed quartz-glass tube from the split-tube furnace used for annealing to an adjacent furnace maintained at 175^{o}C. A field of 1000 V/cm was gradually applied and the crystals slowly cooled through the Curie temperature (4 to 6^{o}C/hour) and then to room temperature before removing the field. This procedure eliminated the need for repoling after the high temperature anneal.

The effects of oxidation (1atm) and reduction (10^{-4}atm) on pure, 50, 500, and 1000ppm Fe-doped samples are shown in Figures 9 (a)-(d). Oxidation increased the height of the broad visible absorption band, turning the more heavily-doped crystals a darker brown and the lightly-doped crystals a slightly deeper yellow or amber. The effect of reduction

was to drastically reduce the height of the 620nm band, changing the heavily-doped crystals from brown to yellow while leaving the high-purity crystal almost colorless.

An interpretation of Figures 8 and 9 can be based on the previous identification of charge transfer bands in $SrTiO_3$ and on the observed Fe-concentration and P_{O2}-dependent trends. The broad absorption band in the visible would then correspond to an Fe^{4+} charge transfer band, with the 620nm (2.0eV) shoulder corresponding to the 590nm feature in $SrTiO_3$:Fe. The shoulder in $BaTiO_3$is shifted to slightly longer wavelength due to differences in the crystal field. The analog to the 440nm peak in the $SrTiO_3$ spectrum occurs at absorbances out of the range of the spectrometer for the sample thicknesses used (3-4.5mm), and probably explains the apparent shifts in the band edge with increasing Fe content.

Qualitatively, the interpretation above conforms well with the proposed defect model. In the as-grown condition the Fe ions are present in both trivalent and tetravalent states, and the relative concentration of Fe^{4+} increases with increasing iron content. This manifests itself as a non-linear increase in the 620nm absorption peak with increasing Fe content observed in Figure 8(b). Upon oxidation, more of the Fe^{3+} is converted to Fe^{4+}, and vice-versa upon reduction, resulting in the trends seen in Figure 9. It is also significant to note that no absorptions corresponding to Fe^{2+} (825nm in $SrTiO_3$) were observed even

for the most reducing conditions investigated herein. This is consistent with the defect model's prediction concerning the low concentration of Fe^{2+} in these samples.

Quantitatively, the Fe-concentration dependence and oxygen-partial-pressure dependence of the 620nm absorption deviate somewhat from the Fe^{4+} concentration behavior predicted by the defect model, but the fit improves with increasing iron content. Figure 10 shows that although the 620nm absorption increases more gradually than predicted for Fe^{4+} at low Fe concentrations, the 3/2 slope predicted by Equation (18) is closely followed in samples where the 620nm shoulder can be resolved (>500ppm Fe). Similarly, the P_{O2} dependence of the 620nm absorption coefficient plotted in Figure 11 is low in lightly-doped samples, but approaches the 1/4 slope predicted for Fe^{4+} (Equation 15) in the 500 and 1000ppm Fe-doped samples.

PHOTOREFRACTIVE MEASUREMENTS

High-purity and Fe-doped $BaTiO_3$ crystals in the as-grown, oxidized, and reduced condition were characterized using a variety of photorefractive techniques, and the observed trends were correlated with the variations in Fe concentration and valence described above. In all the experiments described below, an argon-ion laser operating in the TEM_{00} mode was used to write diffraction gratings in the samples, and a He-Ne laser (λ = 633nm) was used to generate

the read-qut beam when required. All measurements were taken at room temperature (T = 295^{o}K).

Saturation diffraction efficiency measurements provided a preliminary estimate of the relative magnitude of the photorefractive activity in the various samples. These measurements were applied to high-purity, 50ppm, 500ppm, and 1000ppm Fe-doped crystals in the as-grown condition, and to samples from the same boules which were oxidized (P_{O2} = 1atm) and subsequently reduced (P_{O2}= 10-4 atm). In these experiments, gratings with a spacing of 2μm (λ = 514.4nm, 2θ = 14^{o}, and grating vector lying in the plane containing the c-axis) were written in the samples, and the intensity of the diffracted read-out beam was recorded as a function of time until saturation was reached. The results for the 500ppm Fe-doped crystal are shown in Figure 12, indicating that the saturation diffracted beam intensity dropped by almost a factor of ten upon oxidation, while increasing by a lesser degree upon reduction. Similar results were obtained for the 50ppm and 1000ppm samples.

Additional saturation diffraction efficiency measurements were performed on the as-grown and reduced samples in which the data were normalized with respect to the incident intensity (1 μW/cm^2) of the 633nm readout laser beam. The writing beams in this case were of wavelength 488nm with intensities I_1 = 17μW/cm^2 and I_2 = 870μW/cm^2 and were combined at an external angle 2θ = 27^{o} using the anisotropic configuration (grating vector $\vec{K} \perp c$). The

diffracted beam intensities were measured by an EG&G photodiode. All samples were co-polished to identical thicknesses of 4.5mm±3% to allow direct comparison of the results, which are shown in Figure 13 as a function of Fe concentration.

Two-beam coupling measurements were used to determine the sign of the dominant carrier and the effective trap density for the pure as-grown and reduced crystals. In these experiments, the pump and signal beam (λ = 488nm) were ordinary polarized with intensities of I_p = 150 mW/cm^2 and I_S = 180 μW/cm^2 respectively, thus keeping the modulation index $m=2(I_pI_S)^{1/2}/(I_p+I_S)$ small ($m \ll 1$) for compatibility with the standard photorefractive models.[13,40,41] Under these conditions the coupling gain Γ of the two beams is defined by the equation[13]

$$\Gamma = \frac{\cos\theta_i}{l} ln\left(\frac{I_s^p}{I_s^{np}}\right) \tag{21}$$

where I_S^p and I_S^{np} are the intensities of the signal beam with and without the pump beam respectively, l is the crystal thickness, and θ_i is the angle of the beams inside the crystal. The gain of Equation (21) can be expressed by[13,40]

$$\Gamma = \frac{4\pi\delta n}{m\lambda\cos(\theta_i)}, \tag{22}$$

where

$$\delta n = -\frac{n_o^3 E_{sc}}{2} r_{13} \tag{23}$$

and where n_o is the ordinary refractive index, r_{13} is the appropriate electrooptic coefficient, and E_{sc} is the steady state space charge field which has the form[41]

$$E_{sc} = \frac{\varsigma(K)\frac{mkT}{e}}{1+(K/K_0)^2} \tag{24}$$

in which k is Boltzmann's constant, e is the electronic charge, and $\varsigma(K)$ represents the amount of electron hole competition. The term K_0^2 is related to the effective trap density N_T via the equation[13,40]

$$K_0^2 = \frac{e^2 N_T}{\epsilon\epsilon_0 kT}, \tag{25}$$

where ϵ is the relative dielectric constant, and ϵ_0 is the permittivity of free space.

The beam-coupling data is plotted as a function of grating vector K in Figure 14. From the direction of beam coupling it was determined that the charge carriers were positive for both the as-grown and reduced crystals. Fitting this data to the above equations we find that $\varsigma(K)$ is fairly constant over the range of K values used (θ = 2-40°). Using a value of 150 for ϵ_c, the dielectric constant associated with this crystal orientation,[39] we find that the effective trap density is $2.9\pm.4\text{x}10^{16}\text{cm}^{-3}$ and $2.7\pm.5\text{x}10^{16}\text{cm}^{-3}$ for the as-grown and reduced crystal respectively. Note that within the limits of error reduction had no effect on the measured trap density of the high-purity crystals.

Light-induced grating erasure rate measurements were also used to confirm the effective trap densities in the pure samples. This technique has been used previously to determine materials properties of BSO[42] and $BaTiO_3$[13] and involves writing a grating in the crystal using two coherent plane waves, removing the writing beams and flooding the crystal with a uniform erase beam. The decay of the grating diffraction efficiency is simultaneously monitored with a low-power read-out beam. When the modulation index of the fringe pattern and the absorption coefficient are small, the decay rate $1/\tau$ is generally in the form of a single exponential and is related to the grating vector K through the equation[13,40]

$$\frac{1}{\tau} = 2\frac{(\sigma_{ph} + \sigma_D}{\epsilon}\left(\frac{1 + (\epsilon kT/N_T e^2)K^2}{1 + (L_D K)^2}\right) \qquad (26)$$

where σ_{ph} is the photoconductivity, σ_D is the dark conductivity, N_T is the trap density as before, and the diffusion length L_D is given by $L_D^2 = \mu\tau_R kT/e$ where μ is the carrier mobility, and τ_R is the recombination time.

The above experiments were performed for the case of anisotropic diffraction.[43] The writing beams were of wavelength 488nm with intensities I_1 = 200mW/cm^2 and I_2 = 0.1mW/cm^2. The erase beam intensity I_E = 14mW/cm^2 was held constant throughout the experiment since decay rates in $BaTiO_3$ usually exhibit a nonlinear intensity dependence. The readout beam intensity was kept less than 1μW/cm^2. This

readout beam (λ = 633nm) was chopped at a frequency of 1000Hz and the diffracted beam was synchronously detected using a photomultiplier tube and a lock-in amplifier. The output of the lock-in was fed to an AT&T 6300 computer equipped with a Data Translation acquisition board with the sampling rate set at 80Hz. The grating decay data were least-squares fitted to a single exponential and the decay rate $1/\tau$ calculated from the fit. The measurements were repeated as a function of grating vector by varying the writing beam angles.

The decay rates as a function of the square of the grating vector for the range of K values used is shown in Figure 15. Using a value of 3600 for ϵ_a, the dielectric constant appropriate for this orientation,[39] the theoretical fit gives trap density values of $3.1\pm.3\text{x}10^{16}\text{cm}^{-3}$ and $3.3\pm.4\text{x}10^{16}\text{cm}^{-3}$ for the high-purity as-grown and reduced crystals respectively. These values are in good agreement with those obtained for the beam coupling results.

The intensity dependence of the light-induced decay time was also measured for the above high-purity crystals, as well as for the 50ppm and 500ppm Fe-doped crystals in the as-grown and reduced condition. These measurements were conducted at a grating spacing of Λ = 2.8μm, and the results are shown in Figure 16 (a) and (b) for the high-purity and doped crystals respectively. These data show that like the measured trap density, both the intensity dependence and the absolute decay time remained the same in the as-grown and

reduced high-purity crystals. Note also that the addition of large amounts of iron decreases the speed of the crystals, and that this speed is further reduced and the intensity dependence altered by reduction.

DISCUSSION AND CONCLUSIONS

Based on the theoretical defect model for $BaTiO_3$:Fe and on the observed optical absorption spectra, it is apparent that Fe^{3+} and Fe^{4+} are the dominant valence states of iron present in our samples in the P_{O2} range investigated. Thus it is clear that the popular model[5] in which Fe^{3+} and Fe^{2+} are the sources and traps of photorefractive charge carriers does not apply in this case, and that trivalent and tetravalent iron would be expected as the active photorefractive centers if iron plays any role.

Despite the low levels of transition-metal impurities in our high purity $BaTiO_3$ crystals, a relatively strong photorefractive effect was exhibited by these samples. In fact, the effective trap densities determined in the as-grown high-purity samples were on the order of $3x10^{16}cm^{-3}$, which is comparable to those reported for nominally undoped $BaTiO_3$ with two to three orders of magnitude higher impurity levels.[5] Furthermore, upon reduction the effective trap density, carrier sign, and speed were virtually unchanged. Since the defect model predicts that this degree of reduction should yield a nearly seven-fold increase in the concentration of Fe^{3+}, the observed photorefractive behavior

of the high-purity crystals is inconsistent with a model in which Fe^{3+} acts as the trap site for photorefractive carriers. It appears, therefore, that iron is not the dominant photorefractive species in these high-purity $BaTiO_3$ crystals. Instead, these results suggest that the photorefractive traps are associated with a defect whose concentration is independent of oxygen partial pressure in the P_{O2} range 0.21 to 10^{-4} atm. Possibilities for such P_{O2}-independent centers would include barium vacancies or oxygen vacancies (see Figure 7), but these conjectures require further investigation.

Preliminary photorefractive characterization of iron-doped $BaTiO_3$ indicated little change in the saturation diffraction efficiency of the as-grown crystals as a function of Fe content. Even the results for the reduced crystals, which displayed lower overall absorption and slightly higher efficiency, showed no systematic dependence on Fe concentration. The large range of iron concentrations spanned by the data in Figure 14, along with the associated variations in the Fe^{4+}/Fe^{3+} ratio given by Equation (18), offered no visible improvement in properties.

Although the above results seem to suggest that iron centers are not responsible for the photorefractive effect in the doped crystals, it is important to note that the behavior of these samples was different from that of the high-purity crystals. Figure 16 indicates that reduction effected both the speed and the intensity dependence of the

grating erasure process, and that these varied as a function of iron content as well. In addition, the observed decreases and increases in saturation diffraction efficiency which occurred upon oxidation and reduction respectively are not inconsistent with a model involving Fe^{4+} and Fe^{3+} as the sources and traps of photorefractive charge carriers. The interpretation of this data is complicated, however, by a large P_{O2}-dependent absorption coefficient in the Fe-doped crystals. For example, the observed decrease in saturation diffraction efficiency upon reduction may simply be due to increased absorption of the writing beams by non-photorefractive processes.

To further complicate the issue, we have very recently observed evidence of strong intensity-dependent absorption in the Fe-doped crystals as opposed to the high-purity sample which showed none. These observations have inhibited the interpretation of beam coupling and grating decay measurements on the iron-doped crystals, which will be presented elsewhere in the near future. In addition, work is continuing to expand the characterization of the crystals used in this study to cover a wider oxygen partial pressure range in order to further clarify the role of iron centers in the photorefractive process in $BaTiO_3$.

ACKNOWLEDGMENTS

The authors thank Dr. H.-J. Hagemann (Philips GbmH Forschungslaboratorium, Aachen, West Germany) for providing

important thermodynamic data, and Leo Torrenzio (Sanders Associates) for assistance with optical sample preparation. This work was supported by the Army Research Office under contract no. DAAG29-85-K-0057 and by DARPA under contract no. F19628-85-K-0050.

REFERENCES

1. G.C. Valley and M.B. Klein, Optical Engineering, 22(6), 704 (1983).

2. P. Gunter, Physics Reports, 93(4), 199 (1982).

3. F.S. Chen, Journal of Applied Physics, 40(8), 3389 (1969).

4. Sanders Associates, Nashua, N.H.

5. M.B. Klein and R.N. Schwartz, Journal of the Optical Society of America B, 3(2), 293 (1986).

6. G.E. Peterson, A.M. Glass, and T.J. Negran, Applied Physics Letters, 19(5), 130 (1971).

7. G.E. Peterson, A.M. Glass, A.Carnevale, and P.M. Bridgenbaugh, Journal of the American Ceramic Society, 56(5), 278 (1973).

8. M.G. Clark, F.J. DiSalvo, A.M. Glass, and G.E. Peterson, Journal of Chemical Physics, 54(12), 6209 (1973).

9. H. Kurz, E. Kratzig, W. Keune, H. Engelmann, U. Gonser, B. Dischler and A. Rauber, Applied Physics, 12, 355 (1977).

10. B.A. Wechsler, M.B. Klein, and D.A. Rytz, Proceedings of the Society of Photo-Optical Instrumentation Engineers 681, 91-100 (1986).

11. S. Ducharme and J. Feinberg, Journal of the Optical Society of America B, 3(2), 283 (1986).

12. G. Godefroy, G. Ormancey, P. Jullien, Y. Semanou, W. Ousi-Benomar, 1986 IEEE International Symposium on Applications of Ferroelectrics (ISAF), June 8-11, Lehigh University, Bethlehem. PA., paper PA-1.

13. J. Feinberg, D. Heiman, A.R. Tanguay, Jr., and R.W. Hellwarth, Journal of Applied Physics, 51(3), 1297 (1980).

14. P.G. Schunemann, D.A. Temple, R.S. Hathcock, H.L. Tuller, H.P. Jenssen, D.R. Gabbe, and C. Warde, Conference on Lasers and Electro-Optics, Technical Digest Series 14, p.178 (1987).

15. P.G. Schunemann, D.A. Temple, R.S. Hathcock, C. Warde, H.L. Tuller, and H.P. Jenssen, Topical Meeting on Photorefractive Materials, Effects, and Devices, Los Angeles, CA, Technical Digest Series 17, 23 (1987).

16. C. Warde, D. Temple, P. Schunemann, R. S. Hathcock, H.L. Tuller, and H.P. Jenssen, Proceedings of the Society of Photo-Optical Instrumentation Engineers 825, 101 (1987).

17. D.C. Bradley, R.C. Mehotra, and D.P. Gaur, Metal Alkoxides, Ch.3, Academic Press, London (1978).

18. K.B. Wiberg, Laboratory Technique in Organic Chemistry, McGraw Hill, NY, 1-74 (1960).

19. A. Linz, V. Belruss, and C.S. Naiman, Journal of the Electrochemical Society 112, 60C (1965).

20. V. Belruss, J. Kalnajs, and A. Linz, Materials Research Bulletin 6, 899 (1971).

21. A. Glasner and P. Avinur, Talanta, 11, pp. 679, 761, 775 (1964).

22. G. Godefroy, C. Dumas, P. Lompre, and A. Perrot, Ferroelectrics 37, 725 (1981).

23. M.S. Kosman and E.V. Bursian, Soviet Physics Doklady, 2, 354 (1957).

24. G. Ormancey and P. Jullien, Ferroelectrics Letters 1, 103 (1983).

25. J. Blanc and D.L. Staebler, Physical Review B, 4(10), 3548 (1971).

26. H.-J. Hagemann and H.Ihrig, Physical Review B, 20(9), 20 (1979).

27. S.A. Long and R. N. Blumenthal, Journal of the American Ceramic Society, 54(10), 515 (1971).

28. ibid., 54(11), 577 (1971).

29. N.G. Eror and D. M. Smyth, Journal of Solid State Chemistry, 24, 235 (1978).

30. N.-H. Chan, R.K. Sharma, and D.M. Smyth, Journal of the American Ceramic Society, 64(9), 556 (1981).

31. N.-H. Chan and D. M. Smyth, Journal of the Electrochemical Society, 123(10), 1584 (1976).

32. A.M.J.H. Seuter, Philips Research Reports Supplement, 3 (1974).

33. H.-J. Hagemann, A. Hero, and U. Gonser, Physical Status Solidi (a) 61, 63 (1980).

34. H.-J. Hagemann and D. Hennings, Journal of the American Ceramic Society, 64(10), 590(1981).

35. H.-J. Hagemann, "Akzeptorionen in $BaTiO_3$ und $SrTiO_3$ und ihre Auswirkung auf die Eigenschaften von Titanat Keramiken," Ph.D. Thesis, Rheinisch-Westfalische Technische Hochschule Aachen, Federal Republic of Germany, 1980.

36. F.A. Kroger and H.J. Vink, in Solid State Physics, Vol.3, F. Seitz and D. Turnbull (eds.), Academic Press, New York, p. 307 (1956).

37. R. Wernicke, Philips Research Reports, 31, 526 (1976).

38. J.I. Pankove, Optical Processes in Semiconductors, Dover Publications, Inc., NY (1971).

39. S.H. Wemple, M. Didomenico, Jr., and I. Camlibel, Journal of Physics and Chemistry of Solids 29, 1797 (1968).

40. N.V. Kukhtarev, Soviet Technical Physics Letters 2, 438 (1976).

41. F. P. Strohkendl, J.M.C. Jonathon, and R.W. Hellwarth, Optics Letters 11, 312 (1986).

42. R. A. Mullen and R. W. Hellwarth, Journal of Applied Physics 58, 40 (1985).

43. D.A. Temple and C. Warde, Journal of the Optical Society of America B, 3(2), 337 (1986).

FIGURE CAPTIONS

Figure 1. Flow-charts for (a) preparation of high-purity TiO_2 and (b) purification and synthesis of $BaCO_3$.

Figure 2. Typical single crystal boule grown by TSSG.

Figure 3. Photograph of 90 degree domain walls (diagonal lines) in unpoled $BaTiO_3$ single crystal.

Figure 4. Measured ultraviolet spectra of reagent $BaCl_2$ and purified $BaCO_3$ dissolved in HCl. Peak at 230nm corresponds to iron impurities removed by solvent extraction.

Figure 5. Measured optical absorption spectra comparing relative purity of $BaTiO_3$ single crystals grown from commercial and purified feed materials.

Figure 6. Calculated variations in the concentrations of Fe^{2+}, Fe^{3+}, and Fe^{4+} as a function of oxygen partial pressure at various Fe concentrations for an equilibration temperature of $800^{o}C$.

Figure 7. Calculated variations in oxygen vacancy concentration vs. P_{O2} for different Fe doping levels and background acceptor levels given in Table 1.

Figure 8. Measured optical absorption spectra as a function of Fe doping for as-grown crystals after mechanical poling: (a) E parallel to c; (b) E perpendicular to c.

Figure 9. Effects of oxidation (P_{O2} = 1atm, $800^{o}C$) and reduction (P_{O2} = 10^{-4}atm, $800^{o}C$) on the absorption spectra of $BaTiO_3$: (a) High-purity; (b) 50ppm Fe; (c) 500ppm Fe; and (d) 1000ppm Fe (E perpendicular to c).

Figure 10. $Log\alpha_{620}$ vs. $log[Fe]_{tot}$, illustrating the trend toward the theoretical 3/2 dependence at higher Fe concentrations where the 620nm shoulder can be resolved.

Figure 11. P_{O2}-dependence of the 620nm absorption coefficient (Fe^{4+}) approaching the predicted 1/4 slope with increasing Fe content.

Figure 12. Effects of oxidation and reduction on the diffracted beam intensity vs. time for $BaTiO_3$:500ppm Fe. Similar results were achieved for 50ppm and 1000ppm Fe-doped $BaTiO_3$.

Figure 13. Saturation diffraction efficiency of as-grown (solid circles) and reduced (open circles) $BaTiO_3$ as a function of Fe concentration.

Figure 14. Beam coupling gain as a function of grating vector K of high-purity $BaTiO_3$. The solid circles represent the as-grown crystal, the open circles the reduced crystal, and the solid line is the theoretical fit.

Figure 15. Light-induced grating decay rate as a function of the grating vector squared for high-purity $BaTiO_3$ in the as-grown (solid circles) and reduced (open circles) condition. Since the theoretical fits overlapped, only one curve is shown (solid line).

Figure 16. The grating diffraction efficiency decay time as a function of the erase beam intensity for as-grown and reduced $BaTiO_3$: (a) high purity; (b) doped with 50ppm and 500ppm Fe.

Table 1. Spark-source mass spectrographic analysis of reagent precursors, purified feed materials, and resulting $BaTiO_3$ single crystal (Quantities given in ppm atomic).

Element	TiO_2 (unpurified)	TiO_2 (purified)	$BaCl_2$ (unpurified)	Urea (unpurified)	$BaCO_3$ (purified)	$BaTiO_3$
Li^+	0.5		2		1	
B^{3+}	2	3	2	0.2	1	5
Na^+	≤2	≤2	2	0.5	2	≤2
Mg^{2+}	2	2	1	≤1	5	2
Al^{3+}	1	2	2	2	3	0.5
*Si^{4+}	5	5	4	10	4	4
P^{5+}	0.1	0.03	0.2	0.1	0.1	0.05
S^{2-}	<2	<2	<2	<0.5	<2	<2
Cl^-	10	3	Major	2	150	10
K^+	2	2	≤0.2	0.1	2	≤0.1
*Ca^{2+}	3	5	200	3	250	2
$Cr^{3+,2+}$	0.06		≤0.02	≤0.02	0.05	≤0.02
$Mn^{2,3,4+}$					≤0.02	≤0.02
$Fe^{2,3,4+}$	2	0.5	0.3	0.2	1	0.3
$Ni^{2,3+}$	0.3		0.1	≤0.04	≤0.04	0.04
$Cu^{1,2+}$	0.1		≤0.02	≤0.02	0.06	
Zn^{2+}			≤0.1		0.1	
As^{5+}			0.5		0.05	0.1
*Sr^{2+}			30		20	50
*Zr^{4+}	0.1		<0.04		0.1	
Nb^{5+}	0.03					
La^{3+}			0.06		0.06	
$Ce^{3,4+}$			≤0.02		≤0.02	
$Pr^{3,4+}$					≤0.02	
Nd^{3+}					≤0.08	
*Pb^{2+}			≤0.04		≤0.04	

*Isovalent impurities

Table 2. Chemical Analysis of Fe-doped $BaTiO_3$ single crystals. Results indicate a segregation coefficient near unity.

SAMPLE NO.	IRON DOPING LEVEL IN MELT	IRON LEVEL IN CRYSTAL, ANALYZED*
1434	0	0.3 PPM +
1442	5 PPM	<10 PPM
1446	50 PPM	49 PPM
1453	500 PPM	530 PPM
1457	750 PPM	731 PPM
1462	1000 PPM	980 PPM

* ATOMIC ABSORPTION (NORTHERN ANALYTICAL)
\+ SPARK SOURCE MASS SPEC (NORTHERN ANALYTICAL)

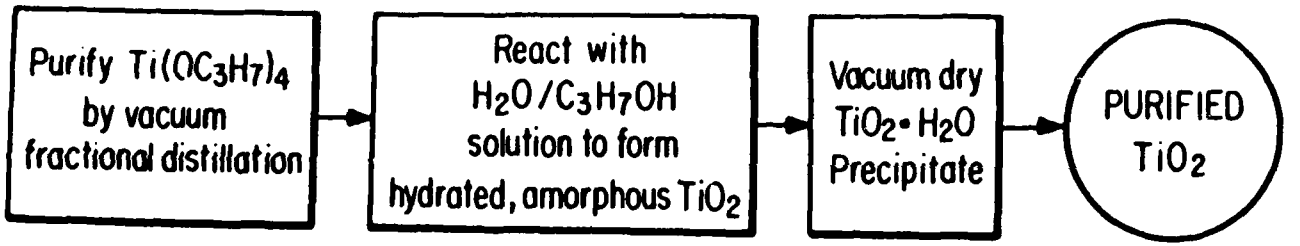

(a) PURIFICATION of TITANIUM DIOXIDE

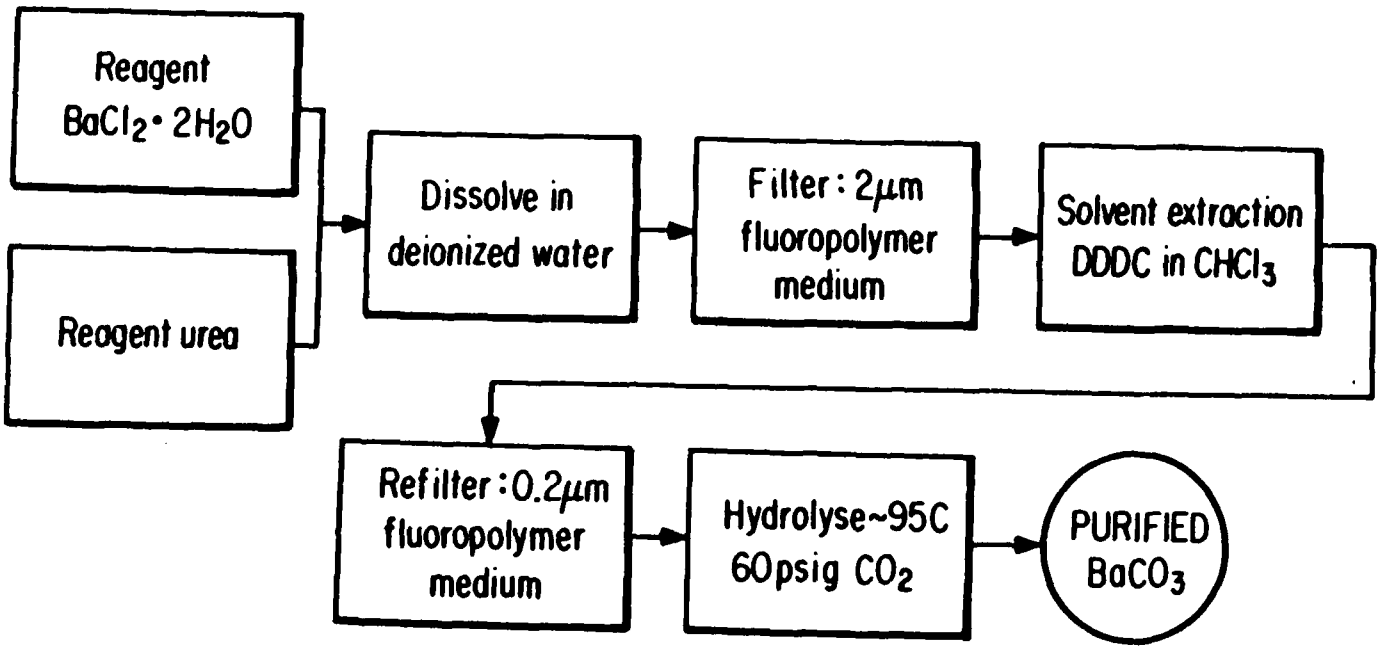

(b) PURIFICATION of BARIUM CARBONATE

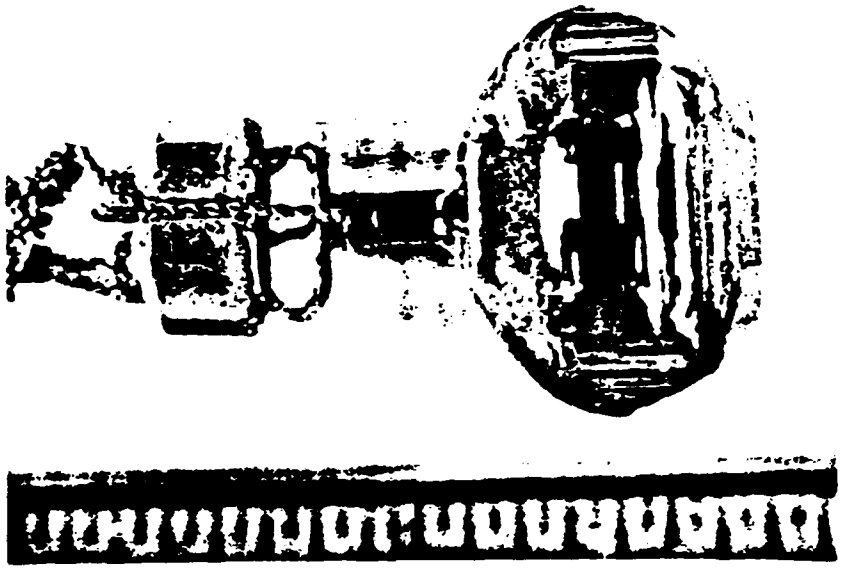

Figure 2. Typical single crystal boule grown by TSSG.

Figure 3. 90 degree domain walls (diagonal lines) in unpoled $BaTiO_3$ single crystal.

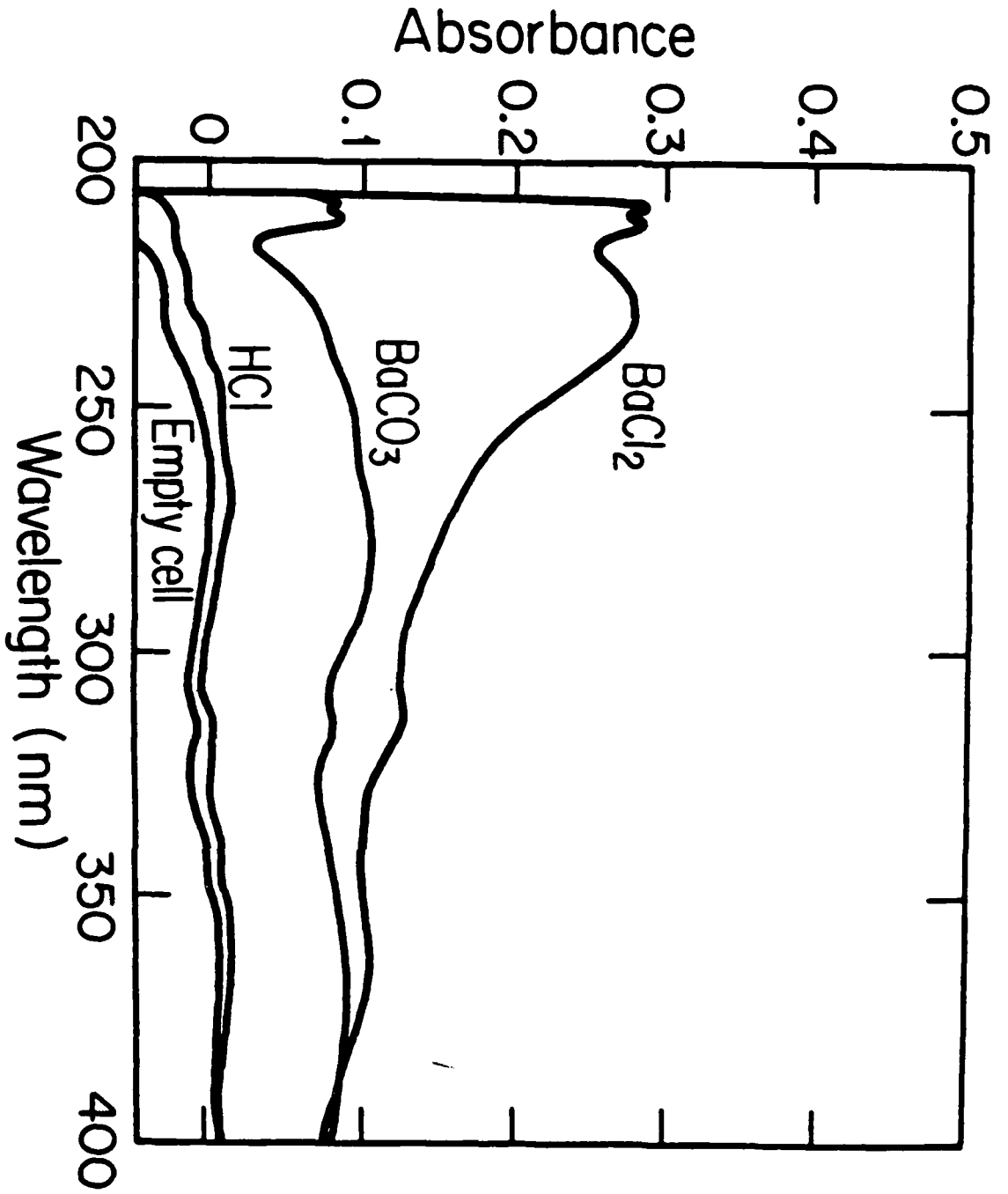
Absorbance
0
0.1
0.2
0.3
0.4
0.5
200
250
300
350
400
Wavelength (nm)
Empty cell
HCl
$BaCO_3$
$BaCl_2$

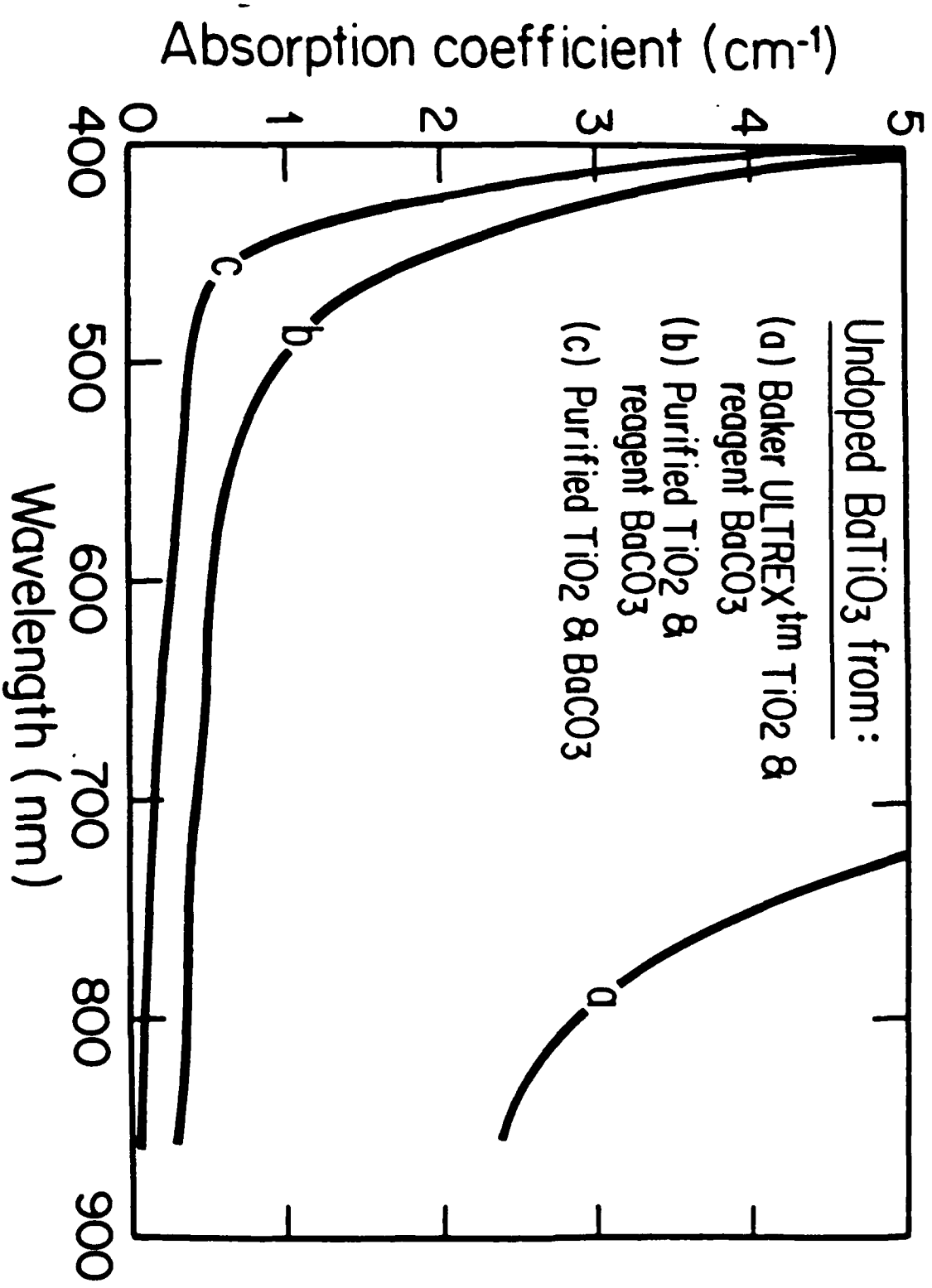
Absorption coefficient (cm-1)
0
1
2
3
4
5
400
500
600
700
800
900
Wavelength (nm)
Undoped BaTiO3 from:
(a) Baker ULTREX tm TiO2 & reagent BaCO3
(b) Purified TiO2 & reagent BaCO3
(c) Purified TiO2 & BaCO3
a
b
c

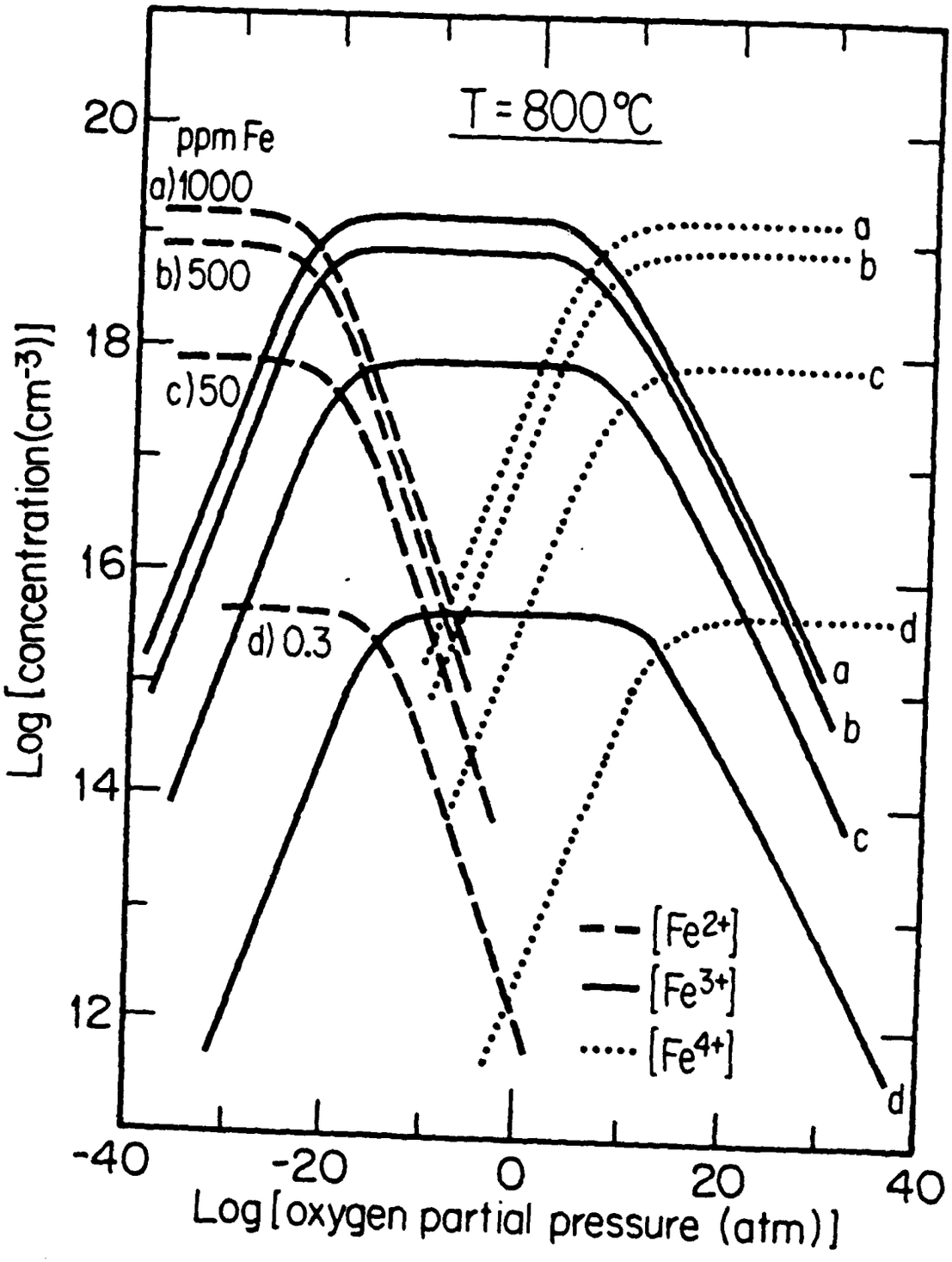
T = 800°C
ppm Fe
a) 1000
b) 500
c) 50
d) 0.3
[Fe2+]
[Fe3+]
[Fe4+]
Log [concentration (cm-3)]
Log [oxygen partial pressure (atm)]
20
18
16
14
12
-40
-20
0
20
40

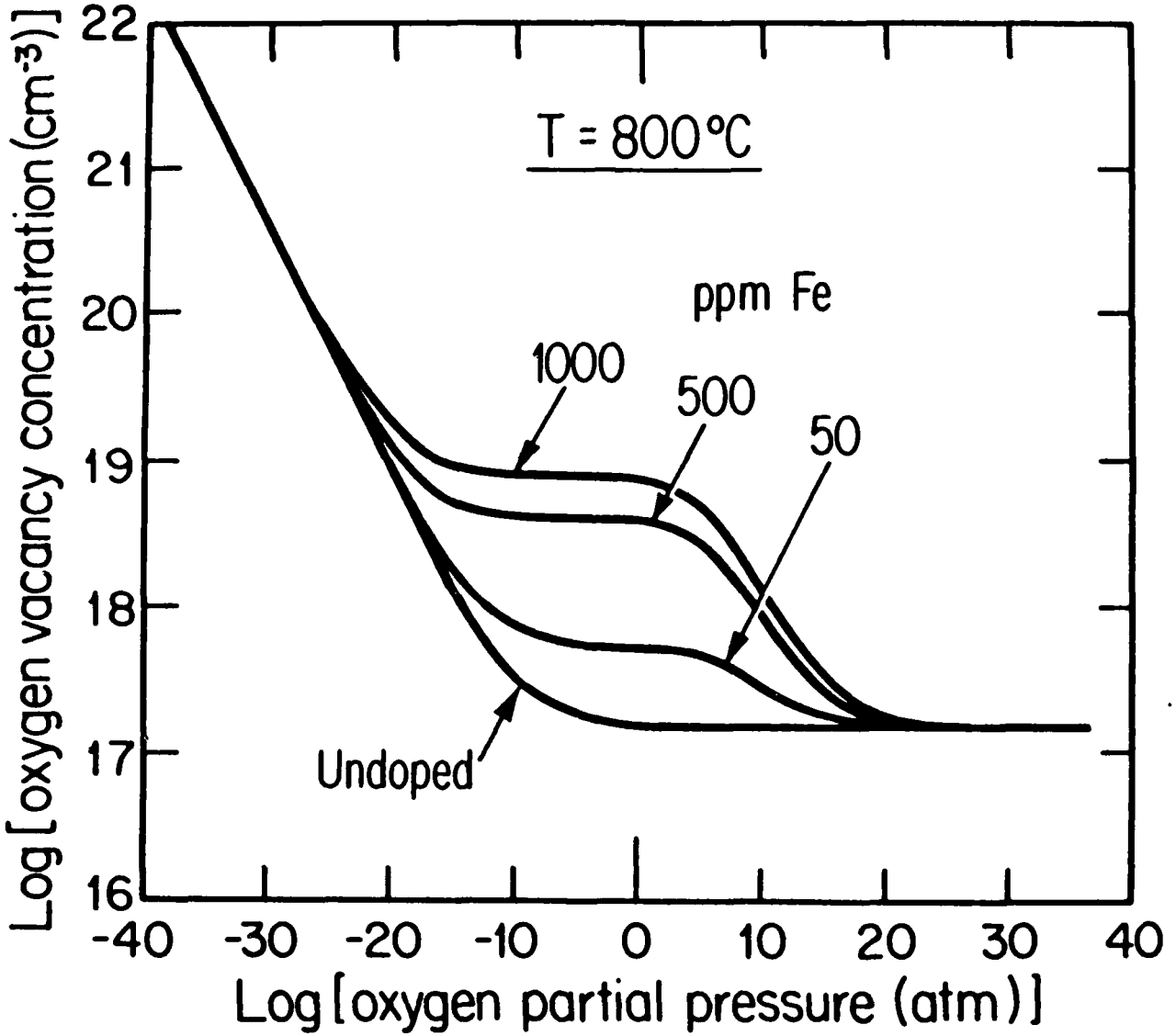
T = 800°C
ppm Fe
1000
500
50
Undoped
Log [oxygen vacancy concentration (cm⁻³)]
22
21
20
19
18
17
16
-40
-30
-20
-10
0
10
20
30
40
Log [oxygen partial pressure (atm)]

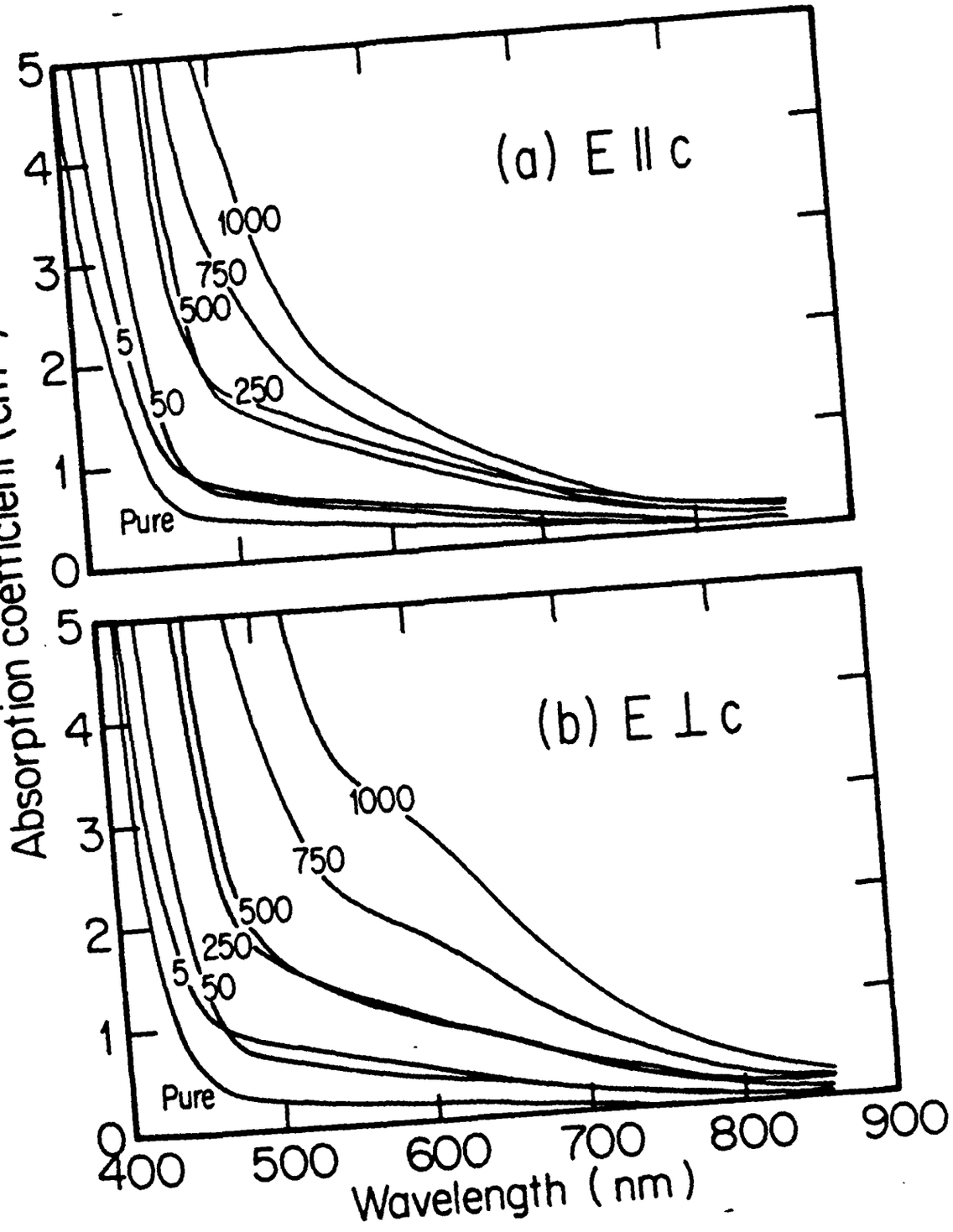
(a) E ∥ c
(b) E ⊥ c
1000
750
500
250
50
5
Pure
Absorption coefficient (cm⁻¹)
Wavelength (nm)
0
1
2
3
4
5
400
500
600
700
800
900

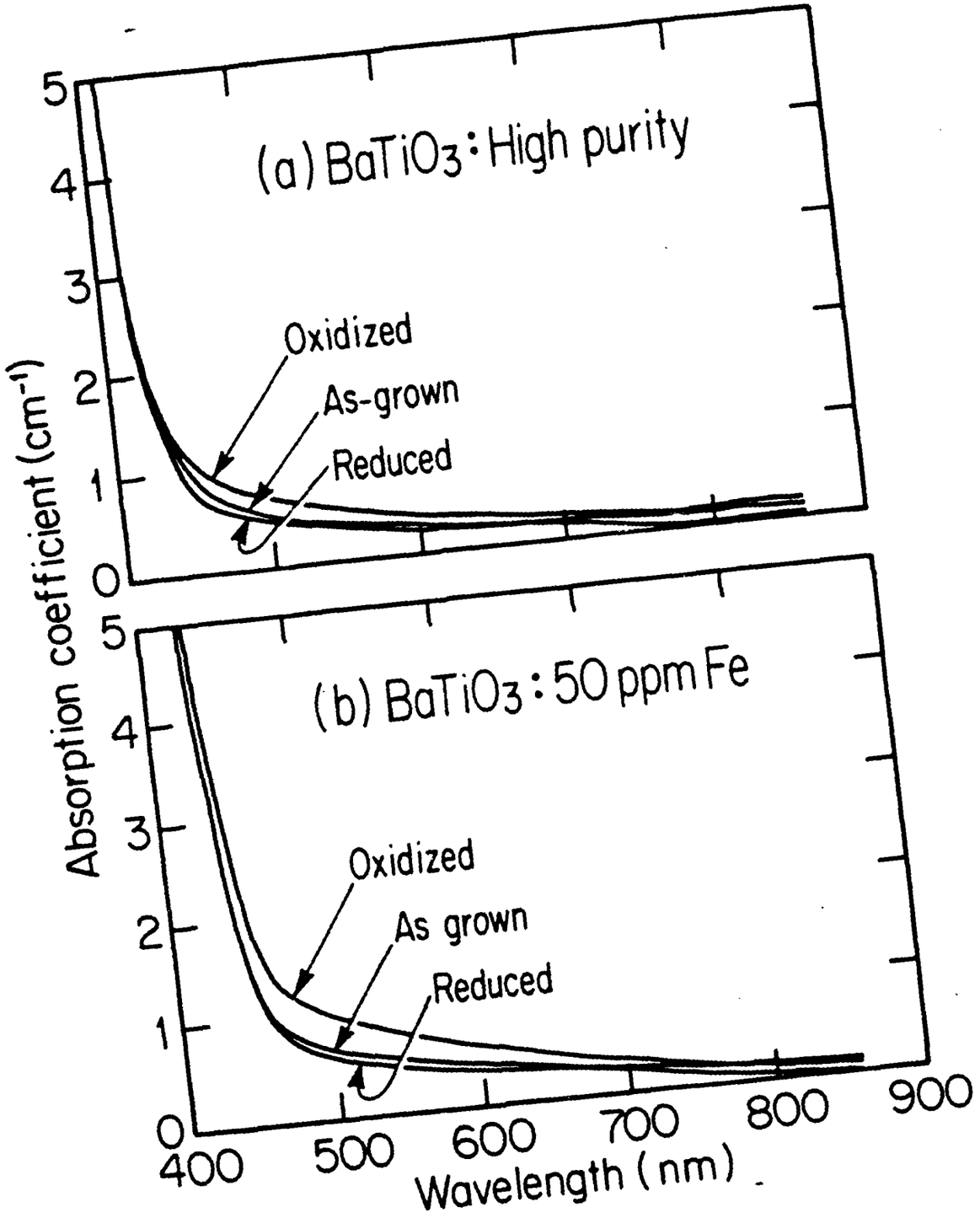
(a) BaTiO3 : High purity
Oxidized
As-grown
Reduced
(b) BaTiO3 : 50 ppm Fe
Oxidized
As grown
Reduced
Absorption coefficient (cm-1)
0
1
2
3
4
5
400
500
600
700
800
900
Wavelength (nm)

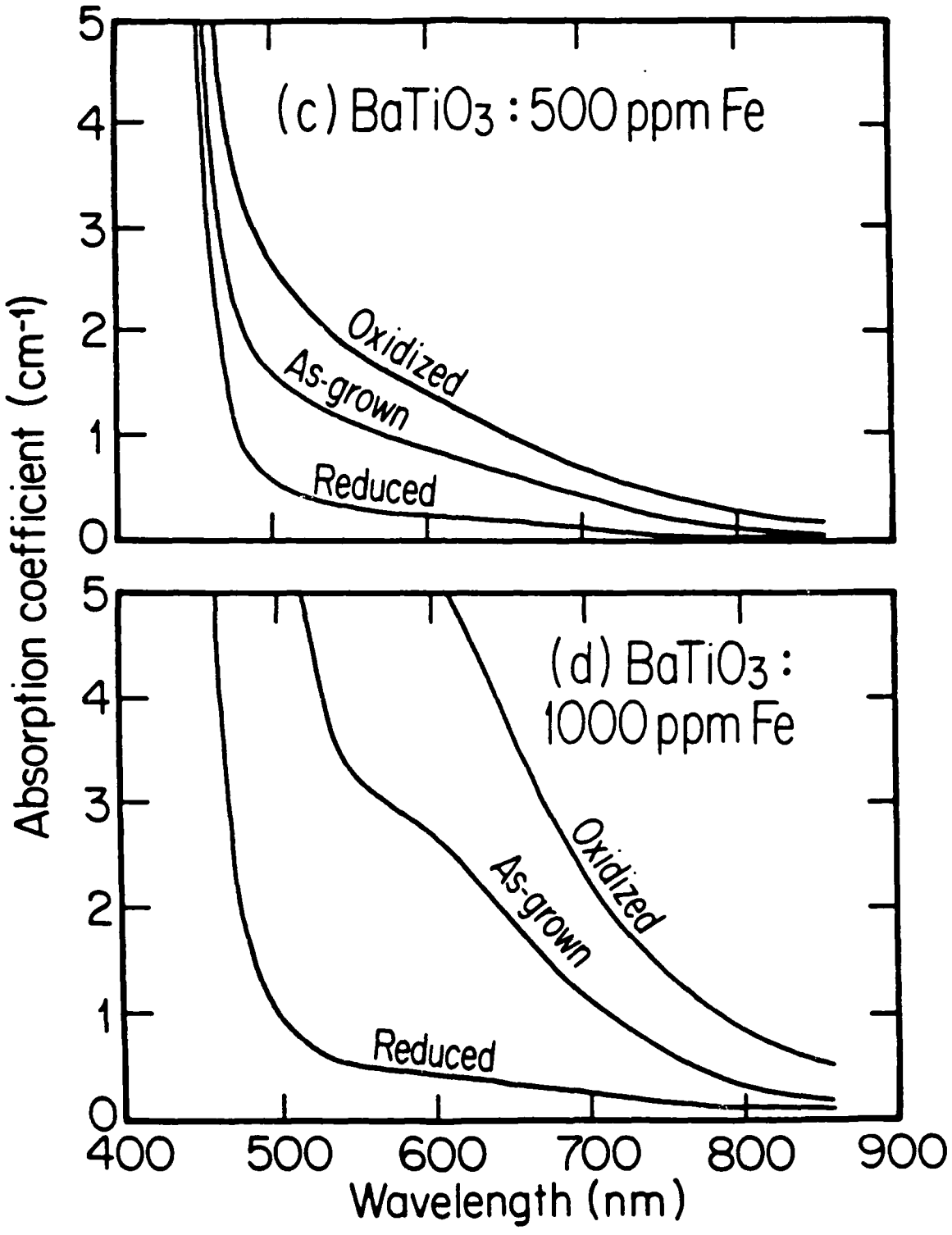
(c) BaTiO3 : 500 ppm Fe
Oxidized
As-grown
Reduced
(d) BaTiO3 : 1000 ppm Fe
Oxidized
As-grown
Reduced
Absorption coefficient (cm-1)
0
1
2
3
4
5
400
500
600
700
800
900
Wavelength (nm)

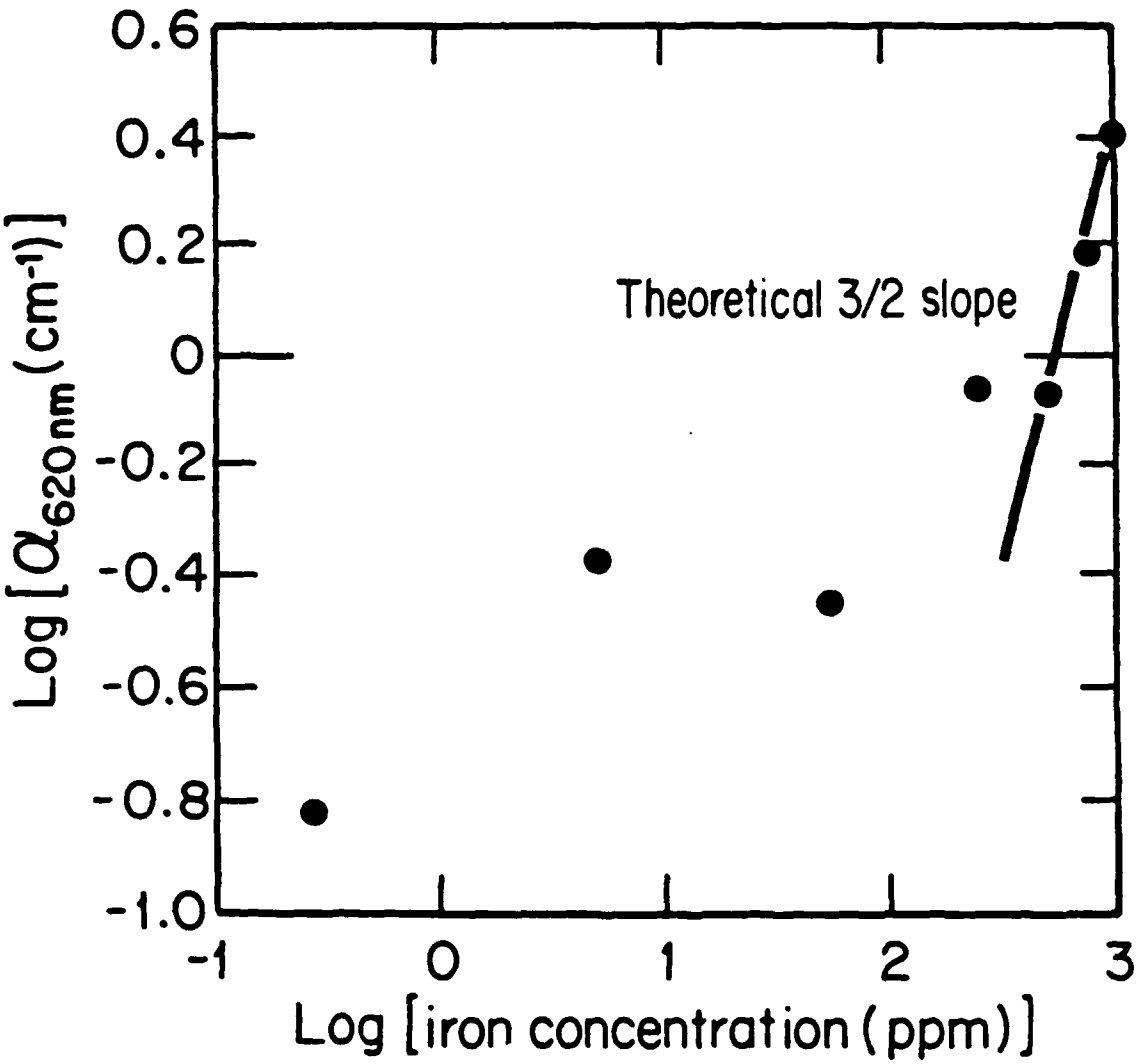
0.6
0.4
0.2
0
-0.2
-0.4
-0.6
-0.8
-1.0
-1
0
1
2
3
Log [α_{620nm} (cm^{-1})]
Log [iron concentration (ppm)]
Theoretical 3/2 slope

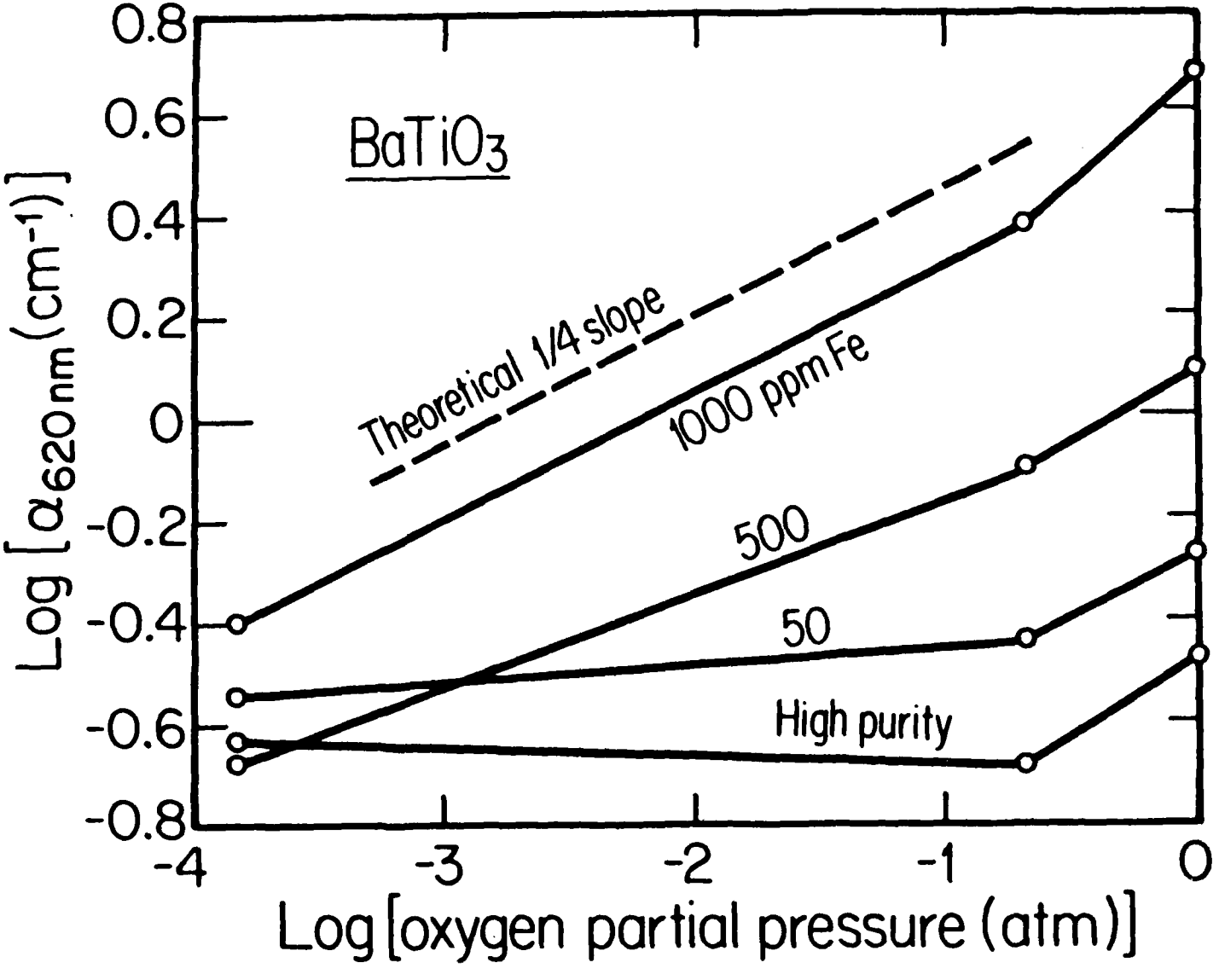
BaTiO3
Theoretical 1/4 slope
1000 ppm Fe
500
50
High purity
0.8
0.6
0.4
0.2
0
-0.2
-0.4
-0.6
-0.8
-4
-3
-2
-1
0
Log [α620nm (cm-1)]
Log [oxygen partial pressure (atm)]

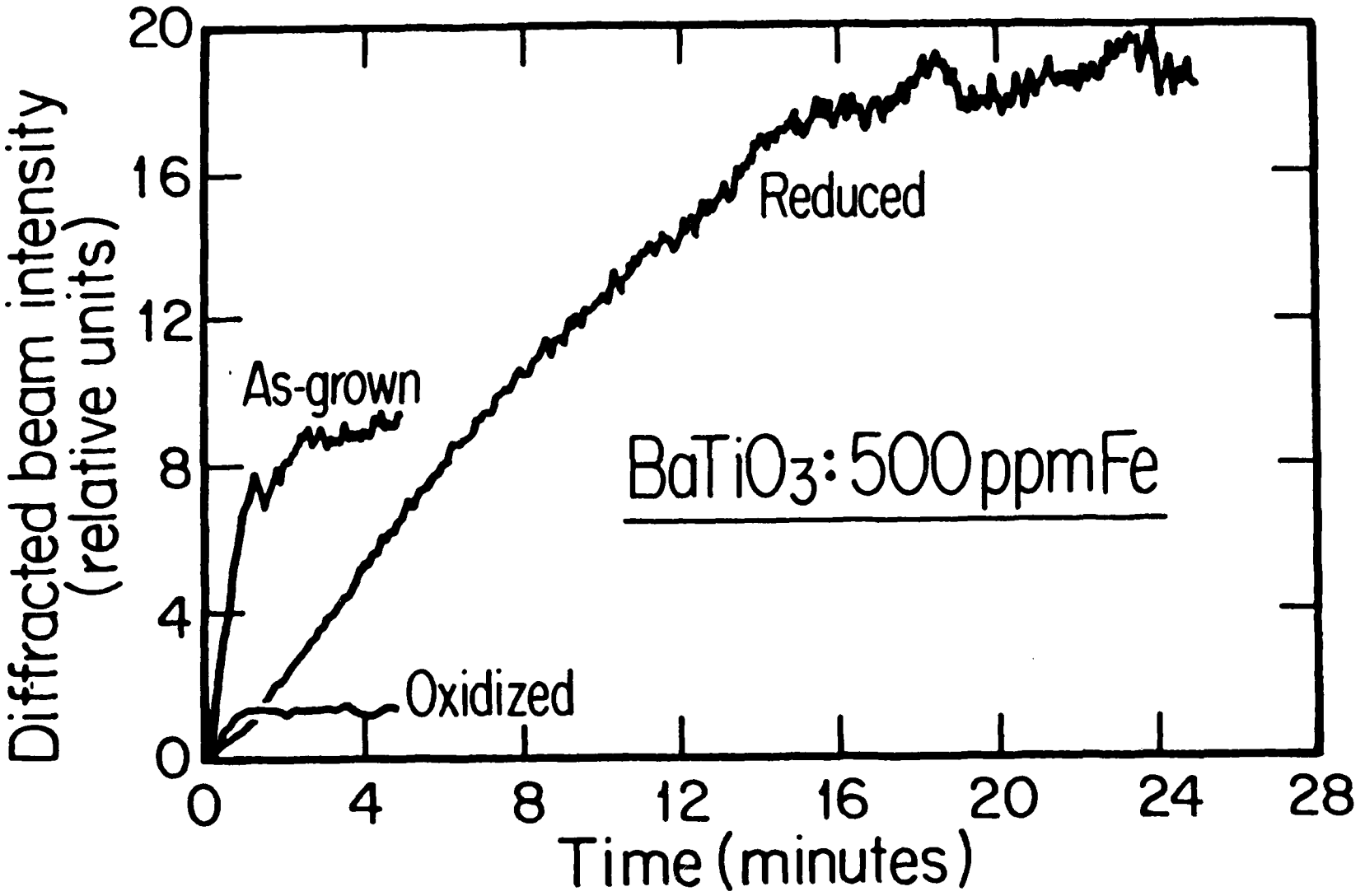
Diffracted beam intensity
(relative units)
20
16
12
8
4
0
0
4
8
12
16
20
24
28
Time (minutes)
As-grown
Reduced
Oxidized
BaTiO3:500ppmFe

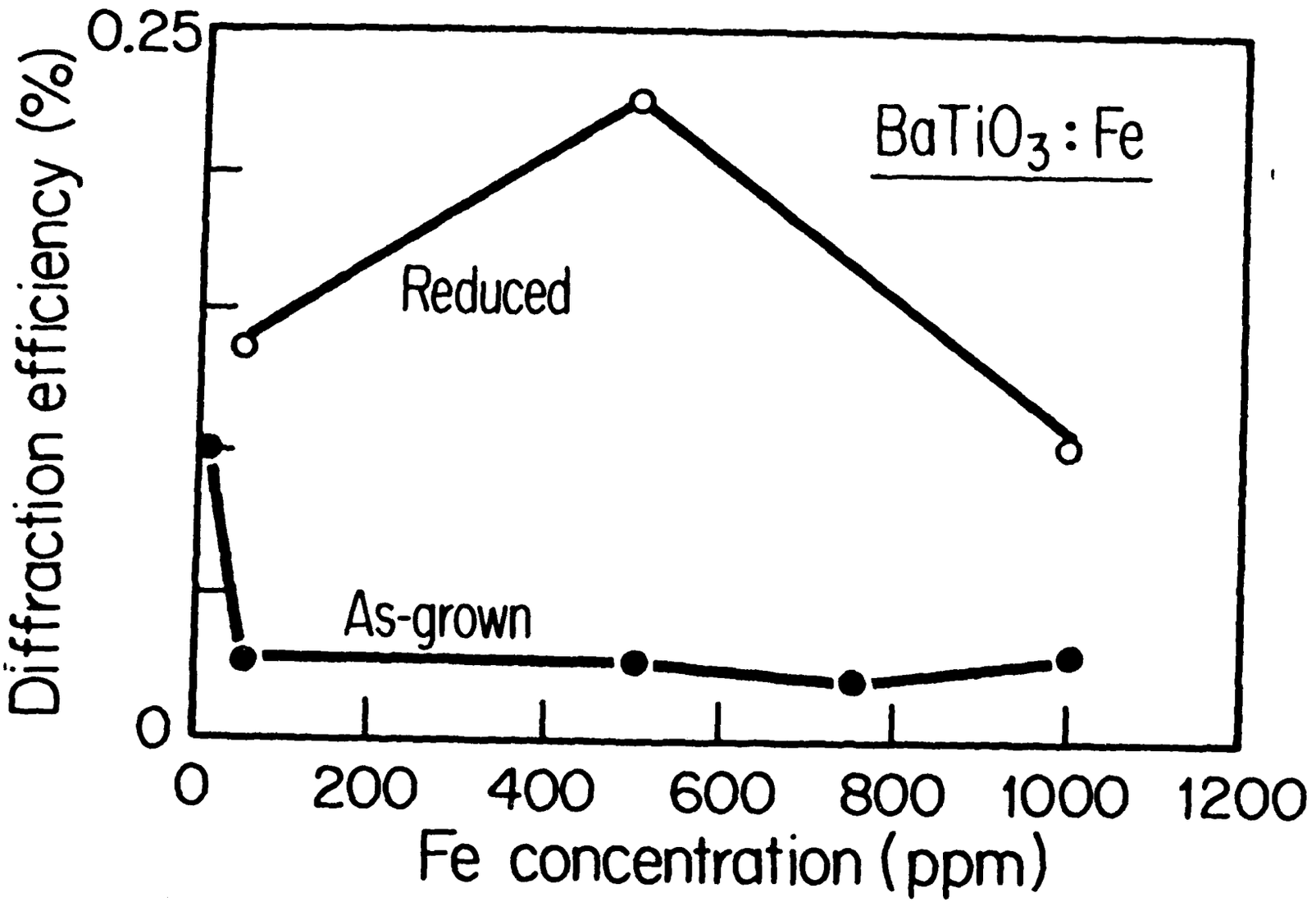
0.25
0
Diffraction efficiency (%)
BaTiO3 : Fe
Reduced
As-grown
0
200
400
600
800
1000
1200
Fe concentration (ppm)

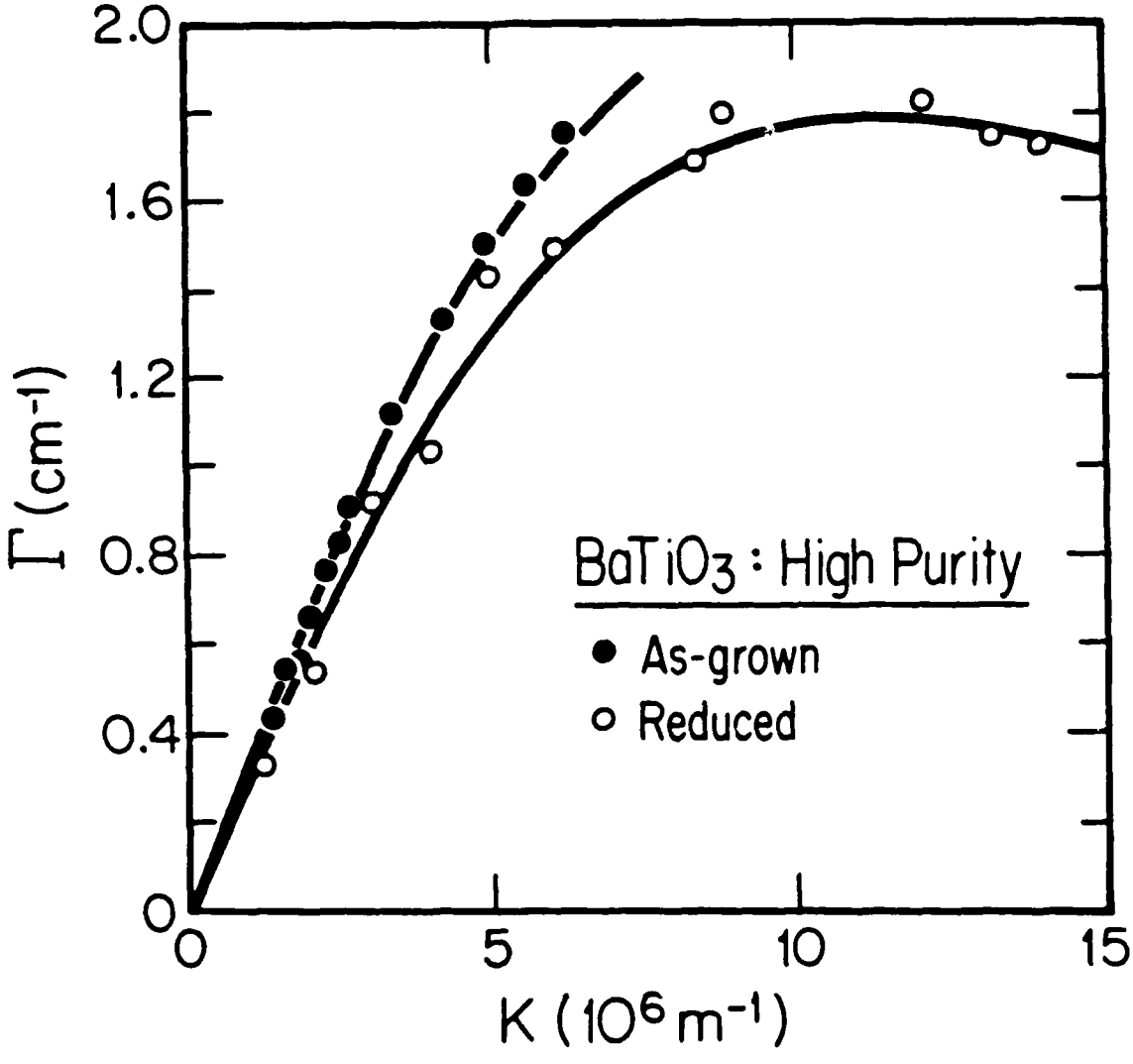
2.0
1.6
1.2
0.8
0.4
0
Γ (cm⁻¹)
0
5
10
15
K (10⁶ m⁻¹)
BaTiO3 : High Purity
As-grown
Reduced

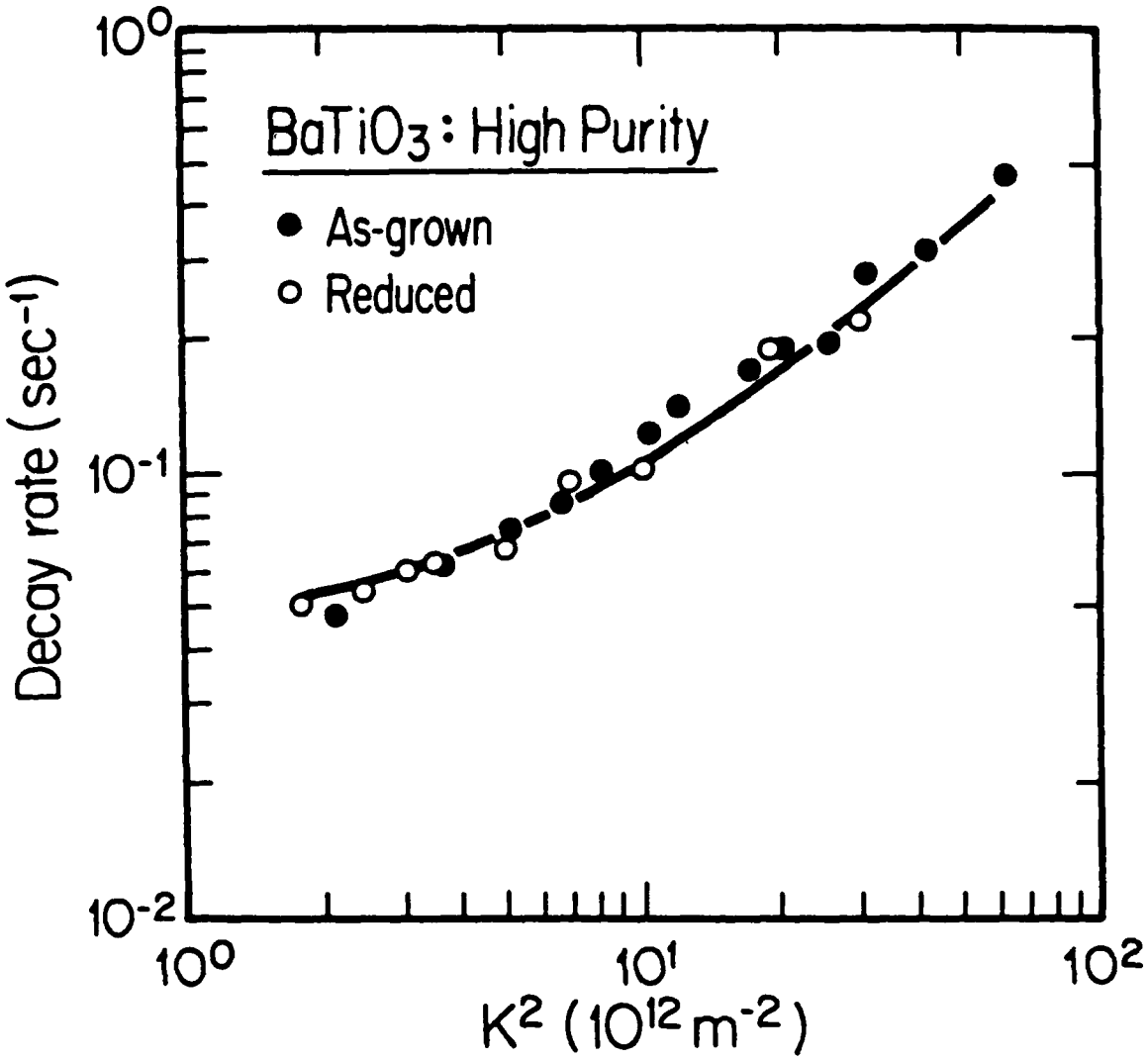
BaTiO3 : High Purity
As-grown
Reduced
Decay rate (sec-1)
10^0
10^-1
10^-2
10^0
10^1
10^2
K^2 (10^12 m^-2)

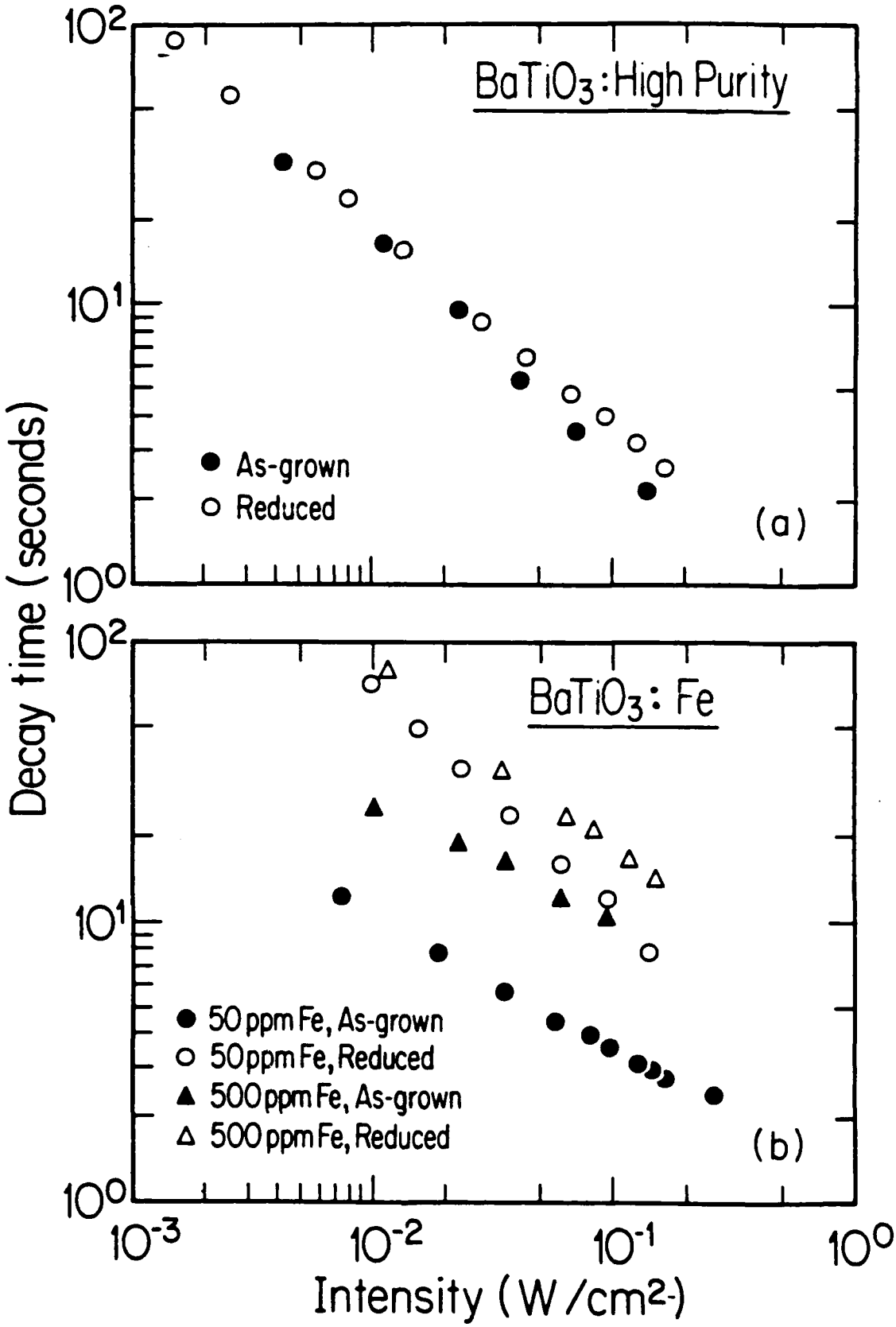
BaTiO3:High Purity
As-grown
Reduced
(a)
BaTiO3: Fe
50 ppm Fe, As-grown
50 ppm Fe, Reduced
500 ppm Fe, As-grown
500 ppm Fe, Reduced
(b)
Decay time (seconds)
Intensity (W/cm2)
10^2
10^1
10^0
10^-3
10^-2
10^-1
10^0

III. Crystal Growth Investigations

1) TSSG Seeding

"Capping", i.e. a region of unstable polycomponent growth underneath the seed, has long been a problem in the growth of $BaTiO_3$. While in most cases it does not prevent the growth of high quality, relatively strain-free crystal, it occasionally causes twinning and cracking. This is a very common problem in solution growth of all types, including hydrothermal growth of quartz and varius types of aqueous solution growth.

A series of growth experiments were run changing various parameters such as seeding temperature, initial temperature lowering rate, diameter, expansion rate and seed rotation rate in an attempt to identify the cause of the cap formation, but with little success. The capping appears to be the result of rapid growth of reentrant faces and consequent trapping of the liquid phase. X-ray analysis of the solidified materials shows the presence of both tetragonal and hexagonal $BaTiO_3$ as well as a third phase which is probably $Ba_6Ti_{17}O_{40}$. In the currently accepted $BaO-TiO_2$ phase diagram, Fig. III-1, this phase form a eutectic with $BaTiO_3$. The fact that the hexagonal phase appears at seeding temperatures ca. 1380° is somewhat surprising since this is well below the reported transition temperature of 1460°. However, we have noticed over the years that growth becomes very difficult above ~1400°C. Even so, the apearance of this phase seems to indicate the presence of fairly large microscale temperature excursions. It is felt that the problem is probably

due to convective instabilities at very small liquid-solid interface, although better temperature control might diminish the problem.

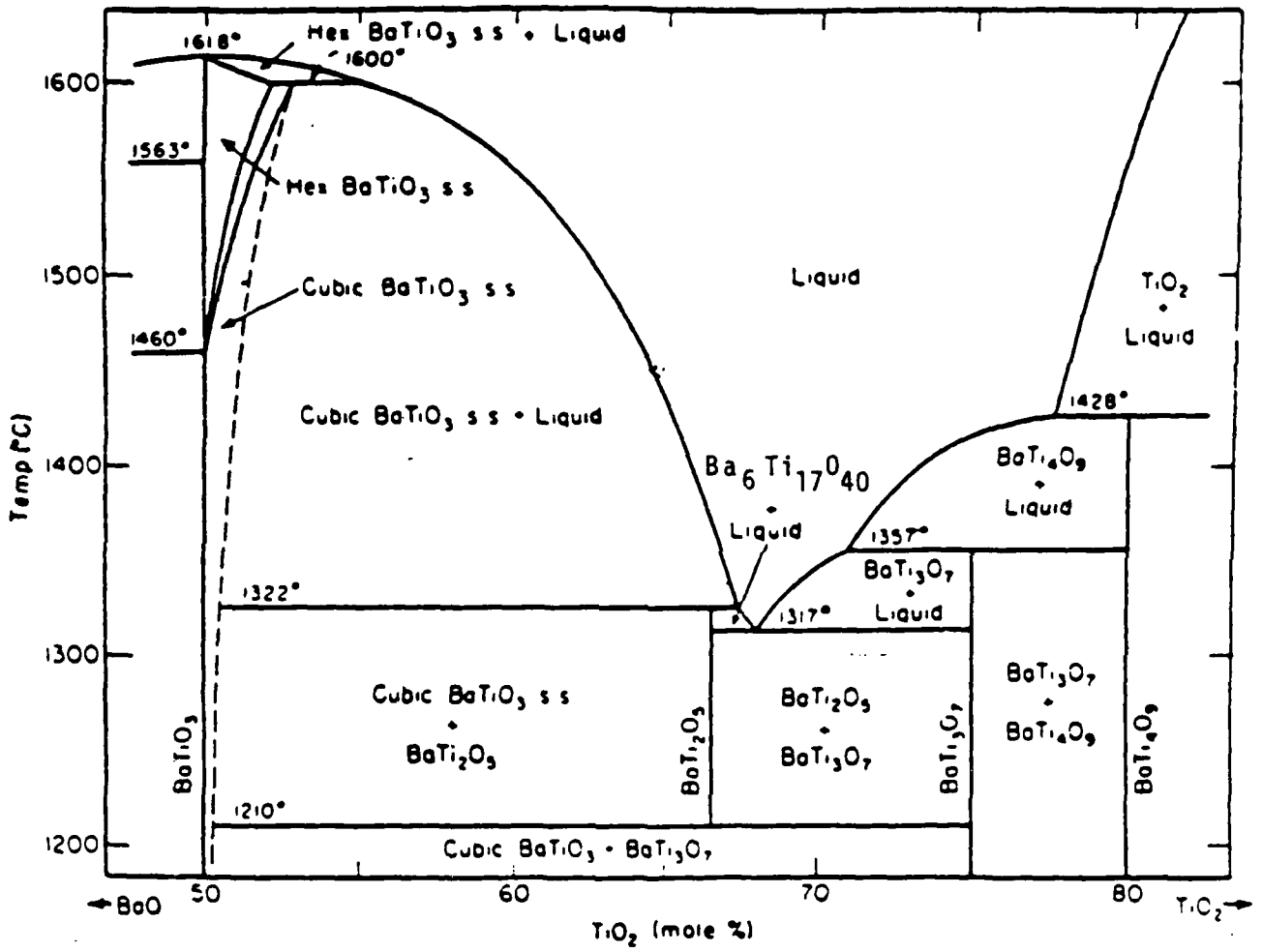

Fig. III-1

Phase diagram of BaO-TiO_3 system after D. E. Rase and Rustum Roy, J. Am. Ceram. Soc. 38, 102-113 (1955), with some modification.

2) RF Furnace Growth

An SiC heated furnace lined with firebrick is inevitably a relatively dirty environment. In contrast, an RF heated Czochralski type furnace can use a minimum of much cleaner (higher purity) refractories, which should result in much less back contamination of the high purity crystal feed material. Much greater control of the temperature gradient is also possible, so that facet-free growth might be obtainable, thus eliminating the "capping" problem discussed in section III-1.

Some preliminary TSSG experiments were run in our recently installed Czochralski furnace. Despite the fact that there was not time to optimize temperature control and, especially temperature gradients, there were indications that this method might be practical. As with other crystals, a reasonably lengthly program of research would be necessary to optimize the crystal growth procedure.